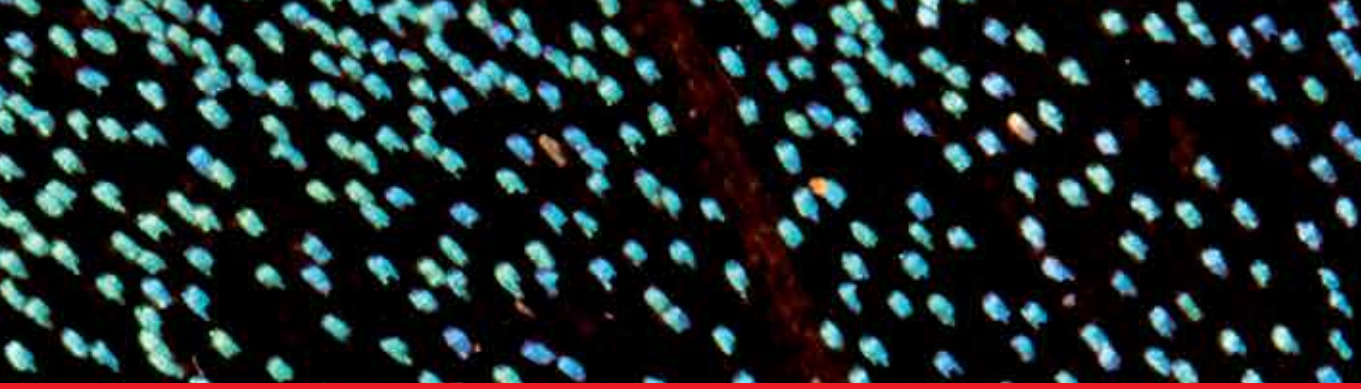

IntechOpen

IntechOpen Book Series
Biomedical Engineering, Volume 2

Non-Invasive Diagnostic Methods

Image Processing

Edited by Mariusz Marzec and Robert Koprowski

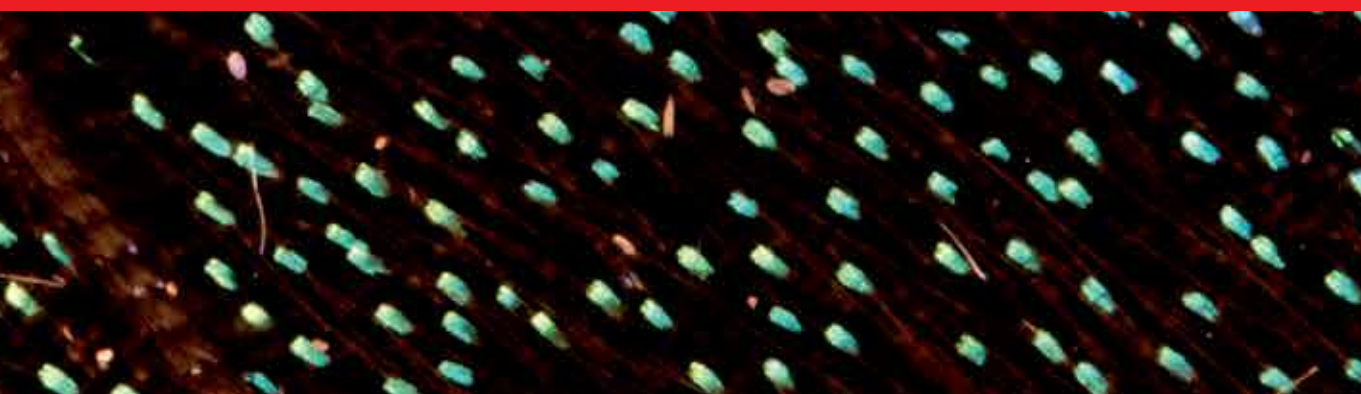

NON-INVASIVE DIAGNOSTIC METHODS - IMAGE PROCESSING

Edited by **Mariusz Marzec**
and **Robert Koprowski**

Non-Invasive Diagnostic Methods - Image Processing
http://dx.doi.org/10.5772/intechopen.76952
Edited by Mariusz Marzec and Robert Koprowski

Part of IntechOpen Book Series: Biomedical Engineering, Volume 2
Book Series Editor: Robert Koprowski

Contributors

Igor Victorovich Lakhno, Alejandro Díaz-Méndez, Patricia Guzmán-Velázquez, Syoji Kobashi, Saadia Alam, Guanghao Sun, Toshiaki Negishi, Tetsuo Kirimoto, Takemi Matsui, Shigeto Abe, Mariusz Marzec

Notice

First published in London, United Kingdom, 2018 by IntechOpen
eBook (PDF) Published by IntechOpen, 2019
IntechOpen is the global imprint of INTECHOPEN LIMITED, registered in England and Wales, registration number: 11086078, The Shard, 25th floor, 32 London Bridge Street
London, SE19SG – United Kingdom
Printed in Croatia

British Library Cataloguing-in-Publication Data
A catalogue record for this book is available from the British Library

Additional hard and PDF copies can be obtained from orders@intechopen.com

Non-Invasive Diagnostic Methods - Image Processing
Edited by Mariusz Marzec and Robert Koprowski

p. cm.

Print ISBN 978-1-78984-844-1

Online ISBN 978-1-78984-845-8

eBook (PDF) ISBN 978-1-83881-837-1

ISSN 2631-5343

IntechOpen Book Series

Biomedical Engineering

Volume 2

Mariusz Marzec is an assistant professor in the Department of Biomedical Computer Systems at the Institute of Computer Science, Silesian University in Katowice. His scientific interests have been focused on computer analysis and processing of images, biomedical images, databases and programming languages. He received his PhD degree in Computer Science in 2012 from the Silesian University of Technology for his dissertation on the use of image analysis and processing for infrared and visible light images in medicine. Dr Marzec is an author and co-author of scientific publications in analysis and processing of biomedical images and developing database systems.

Editor of Volume 2:
Mariusz Marzec
University of Silesia, Poland

Robert Koprowski, MD (1997), PhD (2003), Habilitation (2015), is a lecturer at the Department of Biomedical Computer Systems, Institute of Computer Science, University of Silesia, Poland. For 20 years, he has been dealing with analysis and processing of biomedical images with a particular emphasis on the full automation of measurement for a large inter-individual variability of patients. He is the author of dozens of papers with an impact factor (IF) and more than a hundred of other papers as well as the author or coauthor of six books. Additionally, he is the author of several national and international patents in the field of biomedical devices and imaging. Since 2011, he has been a reviewer of grants and projects (including EU projects) in the field of biomedical engineering.

Book Series Editor and Co-editor of Volume 2:
Robert Koprowski
University of Silesia, Poland

Scope of the Series

Biomedical engineering is one of the fastest growing interdisciplinary branches of science and industry. The combination of electronics and computer science with biology and medicine has resulted in improved patient diagnosis, reduced

rehabilitation time and better quality of life. Nowadays, all medical imaging devices, medical instruments or new laboratory techniques are the result of the cooperation of specialists in various fields. The series of biomedical engineering books covers such areas of knowledge as chemistry, physics, electronics, medicine and biology. This series is intended for doctors, engineers and scientists involved in biomedical engineering or those wanting to start working in this field.

Contents

Introduction

Chapter 1

Introductory Chapter: Non-Invasive Diagnostic Methods in Medicine

Mariusz Marzec

Additional information is available at the end of the chapter

http://dx.doi.org/10.5772/intechopen.82209

1. Introduction

The main purpose of the book is to present examples of non-invasive methods that allow for automatic analysis of biomedical images and signals. These methods can be used to support diagnosis, therapy and monitoring of patients' health [1, 2]. Moreover, the book discusses some selected solutions enabling observation and assessment of health status with the support of information technology. By means of the described methods, it is often also possible to quantify the health status, which allows for the standardization and increased objectivity of the assessment as well as improved diagnosis. These methods are not inconvenient for the patient, which enables to use them in many cases. The current research of non-invasive diagnostic methods uses, among others, standard X-ray images [3, 4], computed tomography images [5, 6], microtomographic images [7] as well as thermographic and ultrasound images [8, 9]. In addition to human tissue testing and assessment, the results of image processing can be also used to evaluate the quality and correctness of assembly of prosthetic elements, implants and endoprostheses, which may affect the effectiveness of therapy [10, 11].

2. Biomedical signal analysis

The first presented method is monitoring the foetal health based on the observation of cardiotocographic (CTG) signal and heart rate variability (HRV). The study was conducted in 49 women divided into four groups, characterized by different pregnancies and well-being. A group of features describing the condition of the foetus containing information from CTG and HRV was preselected from the examined data set. They were then evaluated on the basis of ROC curves and Spearman correlation, choosing those best correlated with the Apgar score. The STV and

LTV (obtained from CTG) as well as SI and AMO (obtained from HRV) parameters were used for further research. Next, an expert system based on the Mamdani-type fuzzy logic rules was built. Based on the input data in the form of four parameters (STV, LTV, SI, AMO), 16 fuzzy rules (fuzzy rules), the system at the output, indicated foetal well-being. According to the adopted assumptions, the system defined the level of well-being as 'normal' (output values in the range from 0 to 0.4), 'distress' (values in the range from 0.6 to 1.0) and 'indeterminate' (values in the range from 0.4 to 0.6). As a result of the classification of 188 records, 84 with foetal distress were classified correctly (true positives), and only one was classified as normal (false negative). In the other cases, 103 stress-free cases were diagnosed correctly (true negatives). The accuracy in foetal stress prediction was 98.8%. The global efficiency was therefore 0.9882 and specificity was equal to 1. The obtained results confirmed the thesis that effective monitoring and observation of the foetus is possible based on data obtained from CTG and ECG apparatuses.

3. Biomedical image analysis

Another example is the method of quantifying the cortical morphological dynamics of brain deformation. The study used data from 105 adult patients, at different ages, from the publicly available OASIS collection. A spatio-temporal statistical shape model (stSSM) was used for the measurement of shape deformation. In order to prepare the model, MR brain images were segmented and edge-based features were generated. Based on these data, the authors prepared mean shapes representing brains of patients in several age groups. On the basis of these models, measurements of instantaneous changes in the shape of the brain over time were made. The selection of the appropriate values of the model operation parameters allowed for a reliable assessment of the correctness of the normal cortical shape evolution for healthy adults. According to the authors, the proposed method can be used not only to create 3D models of the brain but also other organs, i.e. the heart or liver.

The last example is the non-contact method of measuring the heart rate and respiration using a visible light camera and a thermal imaging camera. The basic principles and assumptions that enable to use this type of techniques to assess the health of patients with a suspected infectious disease are discussed here. The research was carried out in a group of 10 students; the cameras were located approximately 50 cm from the subjects' faces. The observations were carried out at rest and after exercises for a period of time equal to 30 seconds. The examination involved simultaneous reading of parameters of breath and electrocardiogram sensors (as reference data) and recording images from visible light and thermal imaging cameras. During respiration, the temperature in the facial area changed, and due to heart beating, the luminance in the facial area also changed. These changes were recorded as a series of images, from which the values representing the current state of the subject in quantitative form were extracted. As a result of the research, it was established that there was a relationship between signals received from the cameras and signals registered by breath and pulse sensors. The obtained results of identification of affected patients (in the study group) indicated the high potential of the proposed solution. According to the authors, the presented solution can be used to prepare an infectious disease screening system. The prediction of positive cases was 100%.

The solutions presented in the book are practical examples of using modern computer technology in the diagnosis, therapy and observation of patients. The application of image analysis and processing methods opens the possibility of automating and accelerating the measurement process. The described research results may be of interest to a wide audience in the field of biomedical engineering.

Author details

Mariusz Marzec

Address all correspondence to: mariusz.marzec@us.edu.pl

University of Silesia, Silesia, Poland

References

[1] Geoff D. Digital Image Processing for Medical Applications. Cambridge University Press, California State University, Channel Islands; 2009

[2] Northrop RB. Noninvasive Instrumentation and Measurement in Medical Diagnosis. Boca Raton: CRC Press; 2001

[3] Jain KR, Chauhan NC. Efficacy of digital image processing techniques in intra oral dentistry. International Journal of Current Engineering and Scientific Research (IJCESR). 2015;**2**(2): ISSN (PRINT): 2393-8374, (ONLINE):2394-0697

[4] Reddy MB, Sridhar V, Nagendra M. Dental X-ray image analysis by using image processing techniques. International Journal of Advanced Research in Computer Science and Software Engineering. 2012;**2**(6):184-189

[5] Seletchi ED, Duliu OG. Image processing and data analysis in computed tomography. Romanian Journal of Physics. 2007;**72**:764-774

[6] Swathi PS, Devassy D, Paul V. Brain tumor detection and classification using histogram thresholding and ANN. International Journal of Computer Science and Information Technologies. 2015;**6**(1):173-176

[7] Boerckel JD, Mason DE, McDermott AM, Alsberg E. Microcomputed tomography: Approaches and applications in bioengineering. Stem Cell Research and Therapy. 2014;**5**(6):144

[8] Lahiri BB, Bagavathiappan S, Jayakumar T, Philip J. Medical applications of infrared thermography: A review. Infrared Physics and Technology. 2012;**55**(4):221-235

[9] Liao AH. Ultrasound in biomedical engineering: Ultrasound microbubble contrast agents promote transdermal permeation of drugs. Journal of Medical Ultrasound. 2016;**24**(3):86-88

[10] Saxena R, Zachariah Santosh G, Sanders Joan E. Processing computer tomography bone data for prosthetic finite element modeling: A technical note. The Journal of Rehabilitation Research and Development. 2002;**39**(5):609-614

[11] Tiossi R, Vasco MAA, Lin L, Conrad HJ. Validation of finite element models for strain analysis of implant-supported prostheses using digital image correlation. Dental Materials 2013;**29**(7):788-796

Section 2

Biomedical Signals Analysis

Chapter 2

Fuzzy Detection of Fetal Distress for Antenatal Monitoring in Pregnancy with Fetal Growth Restriction and Normal

Igor V. Lakhno,
Bertha Patricia Guzmán-Velázquez and
José Alejandro Díaz-Méndez

Additional information is available at the end of the chapter

http://dx.doi.org/10.5772/intechopen.80223

Abstract

Monitoring of fetal cardiac activity is a well-known approach to the assessment of fetal health. The fetal heart rate can be measured using conventional cardiotocography (CTG). However, this method does not provide the beat-to-beat variability of the fetal heart rate because of the averaging nature of the autocorrelation function that is used to estimate the heart rate from a set of heart beats enclosed in the autocorrelation function window. Therefore, CTG presents important limitations for fetal arrhythmia diagnosis. CTG has a high rate of false positives and poor inter- and intra-observer reliability, such that fetal status and the perinatal outcome cannot be predicted reliably. Non-invasive fetal electrocardiography (NI-FECG) is a promising low-cost and non-invasive continuous fetal monitoring alternative. However, there is little that has been published to date on the clinical usability of NI-FECG. The chapter will include data on the accurate diagnosing of fetal distress based on heart rate variability (HRV). A fuzzy logic inference system was designed based on a set of fetal descriptors selected from the HRV responses, as evident descriptors of fetal well-being, to increase the sensitivity and specificity of detection. This approach is found to be rather prospective for the subsequent clinical implementation.

Keywords: fetal non-invasive electrocardiography, fetal heart rate variability, fetal distress

1. Introduction

Electronic fetal monitoring is an important part of the prenatal surveillance system that contributes to the best perinatal outcome. Its objective is the correct evaluation of fetal well-being.

However, the lack of precision of several methods that monitor the fetal well-being is well known [1].

Cardiotocography (CTG) methods have been standard, despite the lack of evidence that it reduces the adverse sequelae of neurodevelopment, including neonatal hypoxic-ischemic encephalopathy and cerebral palsy. This method has a high rate of false positives, and poor inter- and intraobserver reliability [2–4], such that fetal status and the perinatal outcome cannot be predicted reliably.

CTG is a widely available method for fetal development research, based on cardiac rhythm reactivity to fetal intrauterine motor activity in the prenatal period. Doppler ultrasound is the most obvious technological approach for monitoring fetal well-being. However CTG-based techniques require prolonged ultrasonic monitoring.

CTG demonstrates the response of the sinus node to the continuous interaction of the sympathetic and parasympathetic tones of the autonomic nervous system [5, 6]. Autonomic control of fetal cardiac rhythm could be investigated by fetal heart rate variability (HRV). HRV captures the impact of central and peripheral circuits on regulation in hemodynamics [7]. The recording of primary bioelectrical processes in the sinus node can be assumed to be a more valuable technique than the mechanical detection of cardiac cycles used in CTG [1].

The fetal HRV parameters exhibit a wide range, even under normal conditions. The peculiarities of the fetal neurobehavioral response in the active and sleepy periods may complicate the interpretation of the conventional CTG tracing, and increase the level of cesarean interventions [8–10].

Recent research has explored different biochemical and biophysical markers, as well as the correlation between maternal-fetal hemodynamic processes, to better understand the complex processes involved in the loss of fetal well-being [11–20].

The objective of this study is the design of a fuzzy inference system based on a set of fetal descriptors, selected from the CTG and HRV responses, as evident markers of fetal well-being, to increase the sensitivity and specificity in evaluation of fetal distress.

2. Analysis and selection of descriptors

For the development of this study, records of 49 pregnant women were used. These were taken in the Department of Maternal and Fetal Medicine of Kharkiv municipal perinatal center. These records were divided into four groups: Group I composed of healthy pregnant women without loss of fetal well-being, group II of healthy pregnant women with loss of fetal well-being, group III of pregnant women of high-risk type III without loss of fetal well-being, and group IV of pregnant women of high-risk type III with loss of fetal well-being. NI-FECG tracing was obtained from the maternal abdominal wall using the Cardiolab Babycard equipment

(Scientific and research center "KhAI Medica," Ukraine) [1, 11, 12]. The sampling rate was 1000 Hz. For all reported cases, the study protocol was approved by the Bioethics Committee of the Kharkiv Medical Academy of Postgraduate Education (registration number 0105 U002865). For training purposes of fuzzy inference system, the 49 records were divided into windows of 2 minutes to obtain 296 datasets of HRV and CTG parameters.

In order to select the best descriptors to design the fetal well-being inference system, an observation was made using ROC curves and Spearman correlation of the different fetal HRV and CTG parameters used in [12] and shown as the best correlated with Apgar Score 1. These parameters are shown in **Table 1**.

The specificity (Sp) and the sensitivity (Se) of the parameters concerning the fetal well-being were obtained from the ROC analysis. Sp and Se are given by Eqs. (1) and (2), respectively:

$$S_p = \frac{VN}{VN + FP} \tag{1}$$

where VN are the true negatives and FP are the false positives.

Index	Definition
HRV parameters	
SDNN	Standard deviation of normal to normal intervals
RMSSD	Root mean square of successive heart beat interval differences
PNN50	Proportion of the number of pairs of NNs differing by more than 50 ms divided by the total number of NNs
AMO	Mode amplitude (the most frequent value of NN interval of the highest column in the histogram
SI	Stress index
TP	Total power
VLF	Very low frequency
LF	Low frequency
HF	High frequency
CTG parameters	
STV	Short-term variability
LTV	Long-term variability
ACC	Accelerations
DES	Des-accelerations
LOWVAR	Low variability
HIGVAR	High variability

Table 1. HRV and CTG parameters.

$$S_e = \frac{VP}{VP + FN} \tag{2}$$

where VP are the true positives and FN corresponds to the false negatives.

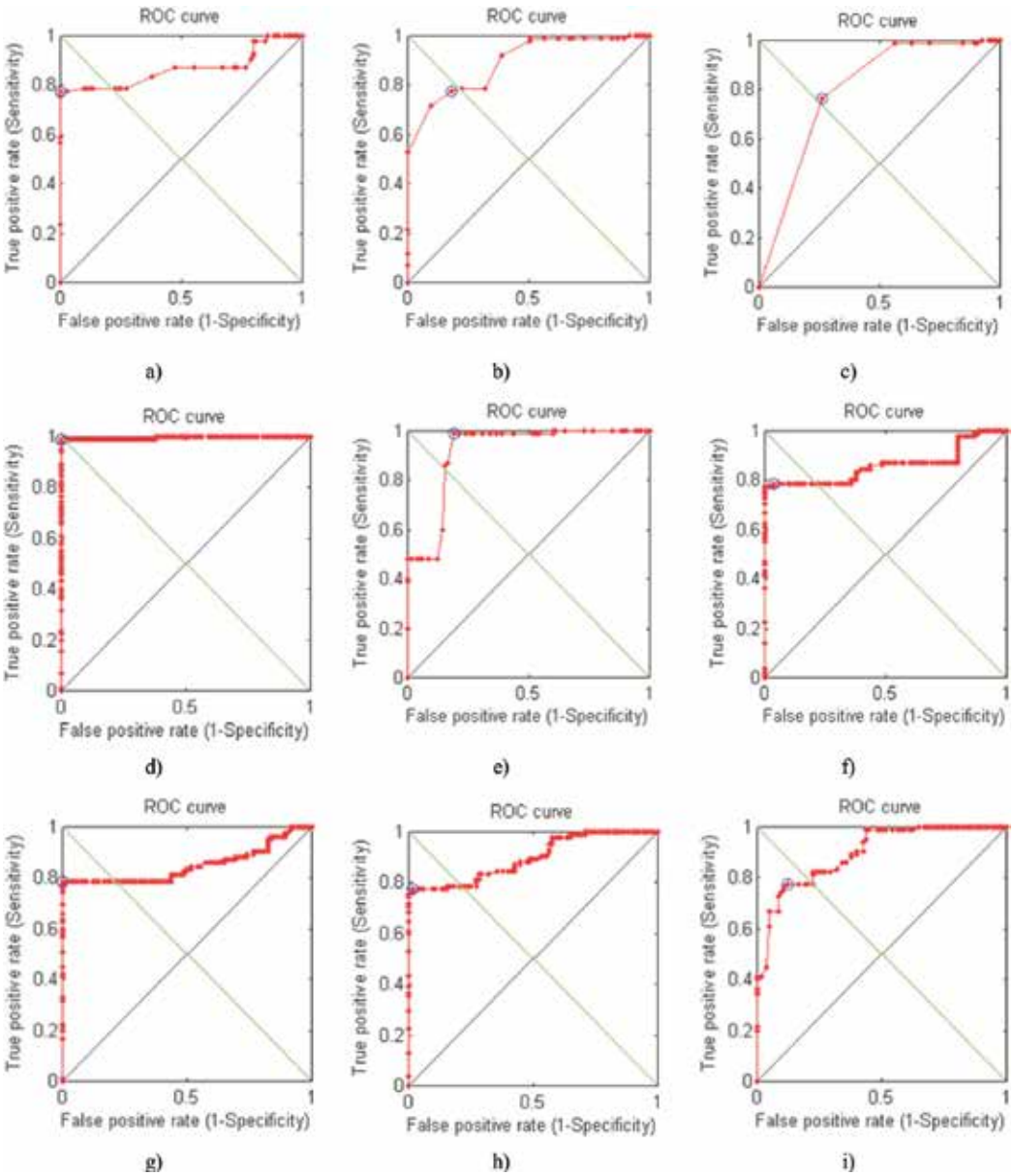

Figure 1. ROC curves for HRV variables. (a) SDNN AUC = 0.8653, (b) RMSSD AUC = 0.8922, (c) pNN50 AUC = 0.7982, (d) SI AUC = 0.9956, (e) AMo AUC = 0.917, (f) TP AUC = 0.8614, (g) VLF AUC = 0.8514, (h) LF AUC = 0.898, and (i) HF AUC = 0.8976.

Spearman's correlation (**ρ**) between bio-signal parameters and well-being fetus state is given by:

$$rs = 1 - \frac{6\sum_{i=1}^{n} d_i^2}{n\left(n^2 - 1\right)} \tag{3}$$

where d_i is the ranges of values for i-parameter and the clinical diagnosis.

Figures 1 and **2** show the ROC curves for the HRV and CTG fetal parameters. As can be seen, the highest AUC is obtained for AMo = 0.9170 and SI = 0.9956 for HRV and, ACC = 0.9974, LTV = 0.9950, STV = 0.9972 and LOWVAR = 0.9922 for CTG. The smallest area was obtained for PNN50 = 0.7982 and DES = 0.6071 for HRV and CTG, respectively.

Table 2 shows the results of the sensitivity, specificity, and Spearman's correlation for HRV parameters which are also shown in **Figure 3**. SDNN, which measures the general variability of the neurovegetative system, showed a high Sp = 1 and a Spearman's correlation of −0.6352,

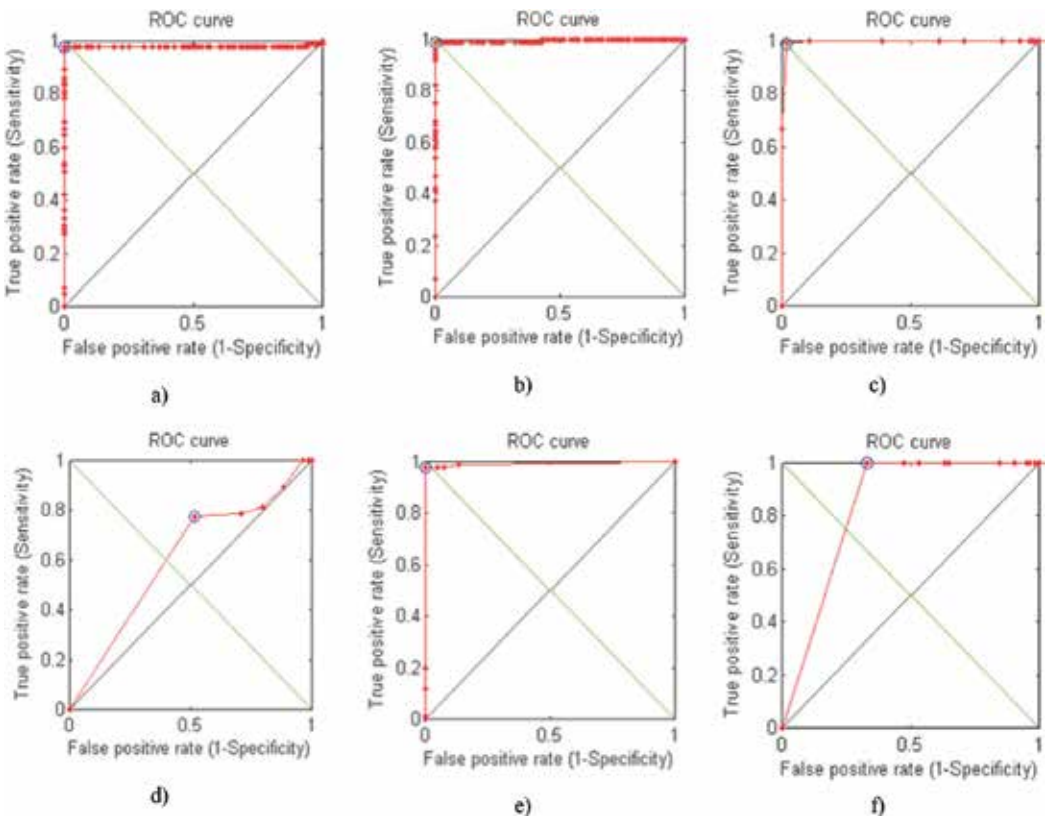

Figure 2. ROC curves for CTG parameters: (a) STV = 0.9772, (b) LTV = 0.9950, (c) ACC = 0.9974, (d) DES = 0.6071, (e) LowVar = 0.9922, and (f) HighVar = 0.8353.

Descriptor	AUC	Sensitivity	Specificity	ρ-Spearman
SDNN	0.8653	0.7765	1	−0.6352
RMSSD	0.8922	0.7765	0.8235	−0.6826
PNN50	0.7982	0.7647	0.7412	−0.5612
SI	0.9956	0.9882	1	0.8585
AMO	0.9170	0.9882	0.8112	0.7243
TP	0.8614	0.7882	0.9647	−0.6262
VLF	0.8514	0.7882	1	−0.6089
LF	0.8980	0.7765	0.9882	−0.6895
HF	0.8976	0.7765	0.8824	−0.6894

Table 2. AUC, sensitivity, specificity, and Spearman's correlation of fetal HRV parameters.

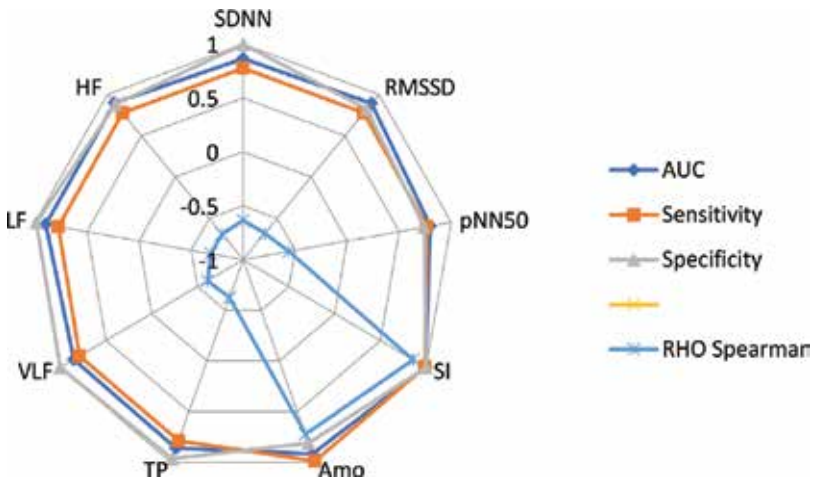

Figure 3. AUC, sensitivity, specificity, and Spearman's correlation of HRV parameters in the study population.

however showed a low value of Se = 0.7765. RMSSD, which is related to high-frequency components, like HF are below 0.90 in the values of both Se = 0.7765 and Sp = 0.8235. TP and LF, although they have a high specificity, 0.9647 and 0.9882 respectively, have a low sensitivity of 0.7882 and 0.7765, respectively. VLF although it has a high specificity Sp = 1 and a Spearman's correlation of −0.6089, its sensitivity is low, Se = 0.7882; HF also presents a low sensitivity of 0.7765. Pnn50 had the lowest sensitivity and specificity Se = 0.7765 and Sp = 0.7412. SI presented Se = 0.9882 and Sp = 1; and AMo showed Se = 0.9882 and Sp = 0.8112. The Spearman's correlation for SI and AMo are, respectively, 0.8585 and 0.7243, which is consistent since SI and AMo are independent of the steady state of the fetus and can be considered evident markers of fetal well-being [12].

In the same way in **Table 3** are shown AUC, Se, Sp, and **ρ** for CTG parameters, these are shown also in **Figure 4**. As can be seen, the highest values were obtained for: STV with a Se = 0.9765, Sp = 1, and **ρ**-Spearman = −0.8271. LTV with a Se = 0.9882, Sp = 1, and **ρ**-Spearman = −0.8579.

Parameter	AUC	Sensitivity	Specificity	ρ-Spearman
STV	0.9772	0.9765	1	−0.8271
LTV	0.9950	0.9882	1	−0.8579
ACC	0.9974	0.9882	0.9882	−0.8826
DES	0.6071	0.7765	0.4824	−0.2176
LOWVAR	0.9922	0.9765	1	0.9218
HIGVAR	0.8353	1	0.6706	−0.6918

Table 3. AUC, sensitivity, specificity, and spearman's correlation of fetal CTG parameters.

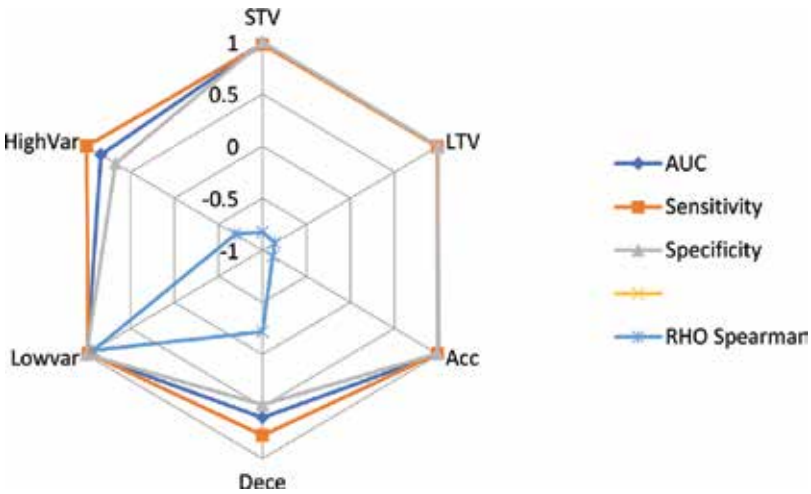

Figure 4. AUC, sensitivity, specificity, and Spearman's correlation of CTG parameters in the study population.

The accelerations (ACC) with Se = 0.9882, Sp = 0.9882, and **ρ**-Spearman = −0.8826. LOWVAR with a Se = 0.9765, Sp = 1, and **ρ**-Spearman = 0.9218. Although HIGHVAR shows a high Se = 1, its Sp is low of 0.6706. The evaluation of short-term variations (STV) and long-term variations (LTV) allow that can be used as markers of fetal compromise.

3. Fuzzy inference system design

The inference system of the fetal well-being state was designed with fuzzy logic, Mamdani-type, 4 inputs (SI, AMo, STV, and LTV), 1 output (status of fetal well-being), and 16 fuzzy rules. The block diagram is shown in **Figure 5**. The fuzzy logic design allows us to take advantage of the linguistic interpretation capacity in complex problems, when there is no simple solution model or a precise mathematical model, such as the detection of loss of fetal well-being. The ranges of selected descriptors are shown in **Table 4**, and were used as the basis for the design of the fuzzy membership functions.

The input variables for fuzzy inference system are SI and AMo for HRV and STV and LTV for CTG. **Figure 6** shows the input membership functions for these variables.

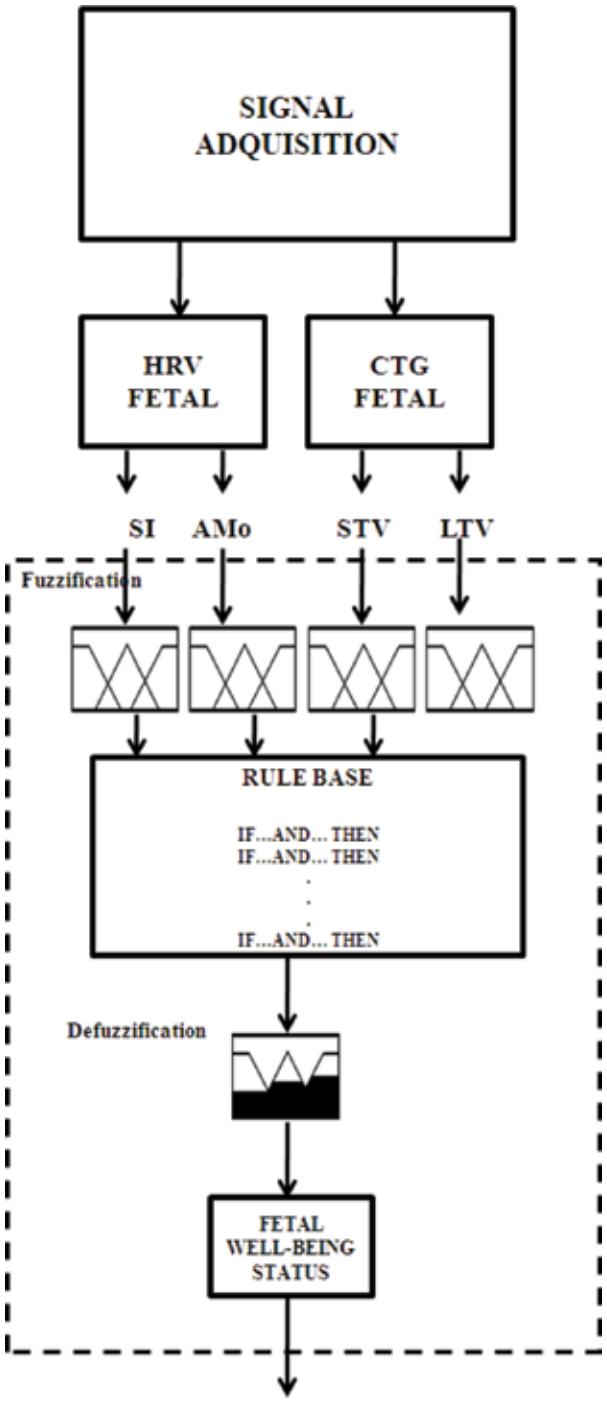

Figure 5. Fuzzy inference system for loss of fetal well-being detection.

Descriptor	Normal	Distress
SI, C.U.	75–2000	1246–3040
AMO, %	29–99	69–100
LTV, MS	26.6–165	14–27.5
STV, MS	5.3–40.4	2.5–6.1

Table 4. Ranges of values of the fetal status descriptors.

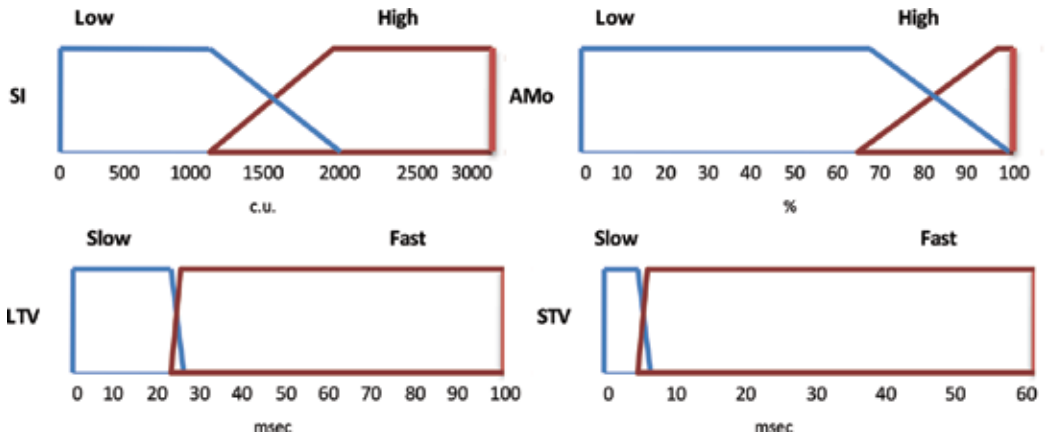

Figure 6. Membership functions for input descriptors: (a) SI, (b) AMo, (c) LTV, and (d) STV.

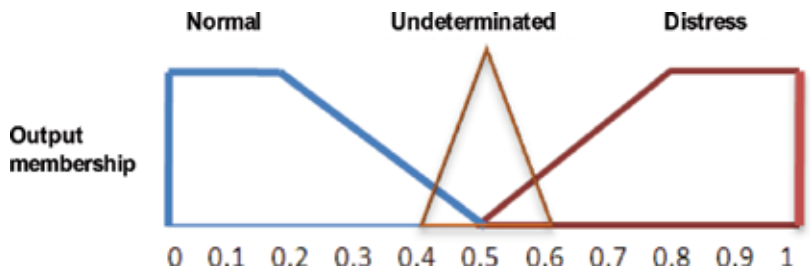

Figure 7. Membership functions for fuzzy system output sets.

The fuzzy output is shown in **Figure 7**, and this is defined by two trapezoidal membership functions, representing normal (N) or distress (D) fetal status, and by a triangular function in which the diagnosis is indeterminate by fuzzy system. The "Normal" output is in the range from 0 to 0.4; for the output "Distress," the rank is of 0.6 to 1.0; and if the output is between 0.4 and 0.6, it is classified as "indeterminate."

The fuzzy knowledge base is shown in **Table 5**. In order to increase the presumption of fetal well-being detection, the inference would have to be "Normal," if and only if, the membership

	SI	AMO	LTV	STV	DX
1	Low	Low	Fast	Fast	Normal
2	Low	Low	Fast	Slow	Undeterminated
3	Low	Low	Slow	Fast	Undeterminated
4	Low	Low	Slow	Slow	Undeterminated
5	Low	High	Fast	Fast	Undeterminated
6	Low	High	Fast	Slow	Distress
7	Low	High	Slow	Fast	Distress
8	Low	High	Slow	Slow	Distress
9	High	Low	Fast	Fast	Undeterminated
10	High	Low	Fast	Slow	Distress
11	High	Low	Slow	Fast	Distress
12	High	Low	Slow	Slow	Distress
13	High	High	Fast	Fast	Undeterminated
14	High	High	Fast	Slow	Distress
15	High	High	Slow	Fast	Distress
16	High	High	Slow	Slow	Distress

Table 5. Fuzzy knowledge base for well-being fetal status.

of the fuzzy sets in the four input descriptors belongs to "Normal" set. On the other hand, the output will be "distress" if the membership in at least one variable of HRV and CTG belong to the input set related to fetal distress. Fuzzy inference can be indeterminate if membership of fuzzy sets in three inputs belongs to sets related to normal fetal status. The "Normal" output is in the range of 0–0.4; "Distress" output range is from 0.6 to 1.0, and the output range from 0.4 to 0.6 will be classified as "Indeterminate."

The fuzzy rules can be written as:

Rule 1. If SI low and AMo low and LTV fast and STV fast, then there is normal fetal well-being.

IF SI↓ AND AMo↓ AND LTV↑ AND STV↑ THEN NORMAL.

Rule 2. If SI low and AMo low and LTV fast and STV slow, then there is unclear diagnosis.

IF SI↓ AND AMo↓ AND LTV↑ AND STV↓ THEN UNDETERMINATED.

Rule 3. If SI low and AMo low and LTV slow and STV fast, then there is unclear diagnosis.

IF SI↓ AND AMo↓ AND LTV↓ AND STV↑ THEN UNDETERMINATED.

Rule 4. If SI low and AMo low and LTV slow and STV slow, then there is unclear diagnosis.

IF SI↓ AND AMo↓ AND LTV↓ AND STV↓ THEN UNDETERMINATED.

Rule 5. If SI low and AMo high and LTV fast and STV fast, then there is unclear diagnosis.

IF SI↓ AND AMo↑ AND LTV↑ AND STV↑ THEN UNDETERMINATED.

Rule 6. If SI low and AMo high and LTV fast and STV slow, then there is fetal distress.

IF SI↓ AND AMo↑ AND LTV↑ AND STV↓ THEN DISTRESS.

Rule 7. If SI low and AMo high and LTV slow and STV fast, then there is fetal distress.

IF SI↓ AND AMo↑ AND LTV↓ AND STV↑ THEN DISTRESS.

Rule 8. If SI low and AMo high and LTV slow and STV slow, then there is fetal distress.

IF SI↓ AND AMo↑ AND LTV↓ AND STV↓ THEN DISTRESS.

Rule 9. If SI high and AMo low and LTV fast and STV fast, then there is unclear diagnosis.

IF SI↑ AND AMo↓ AND LTV↑ AND STV↑ THEN UNDETERMINATED.

Rule 10. If SI high and AMo low and LTV fast and STV slow, then there is fetal distress.

IF SI↑ AND AMo↓ AND LTV↑ AND STV↓ THEN DISTRESS.

Rule 11. If SI high and AMo low and LTV slow and STV fast, then there is fetal distress.

IF SI↑ AND AMo↓ AND LTV↓ AND STV↑ THEN DISTRESS.

Rule 12. If SI high and AMo low and LTV slow and STV slow, then there is fetal distress.

IF SI↑ AND AMo↓ AND LTV↓ AND STV↓ THEN DISTRESS.

Rule 13. If SI high and AMo high and LTV fast and STV fast, then there is unclear diagnosis.

IF SI↑ AND AMo↑ AND LTV↑ AND STV↑ THEN UNDETERMINATED.

Rule 14. If SI high and AMo high and LTV fast and STV slow, then there is fetal distress.

IF SI↑ AND AMo↑ AND LTV↑ AND STV↓ THEN DISTRESS.

Rule 15. If SI high and AMo high and LTV slow and STV fast, then there is fetal distress.

IF SI↑ AND AMo↑ AND LTV↓ AND STV↑ THEN DISTRESS.

Rule 16. If SI high and AMo high and LTV slow and STV slow, then there is loss of fetal well-being.

IF SI↑ AND AMo↑ AND LTV↓ AND STV↓ THEN FETAL DISTRESS.

4. Results

The results of the fuzzy diagnosis for 188 datasets are shown in **Figure 8**. Two well-defined clusters can be observed, corresponding to those who were clinically diagnosed as healthy pregnancies (+) and those who presented loss of fetal well-being (o). Can be observed that a

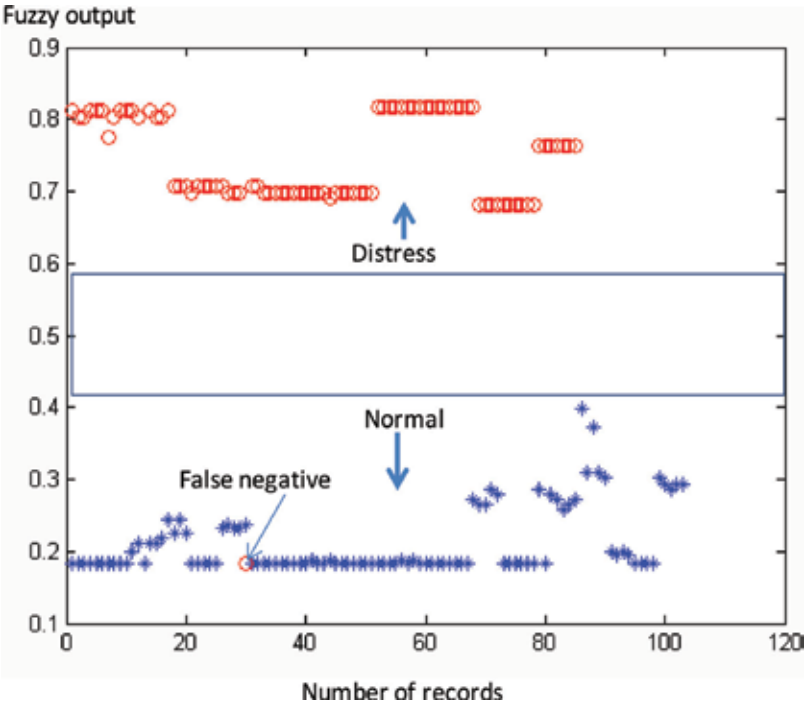

Figure 8. Scatter plot for fuzzy outputs of the 188 records.

fuzzy output from a high-risk pregnancy record with fetal distress was incorrectly evaluated by fuzzy system, fuzzy output of 0.183 classifies it as normal pregnancy.

Table 6 shows 6 of the 49 records, the values for their descriptors, the fuzzy output, and the clinical diagnosis. The records N16, N6, FGR6, FGR29, N27 are well evaluated by the fuzzy inference system, but the record FGR20, which corresponds to a fetal growth restricted pregnancy with fetal distress, is classified by fuzzy system as normal pregnancy. The ROC curve and confusion matrix for the 188 cases evaluated are shown in **Figure 9**.

Of the 188 records, 84 with fetal distress were correctly evaluated (true positives) and only one was diagnosed as normal (false negative). On the other hand, the 103 normal cases were

Record ID	SI	AMo	LTV	STV	Fuzzy output	Clinic DX
N16	1057	75	49.1	12	0.242	Normal
N6	3034	100	14.3	2.7	0.769	Fetal Distress
FGR6	687	77	49.2	9.5	0.247	Normal
FGR 29	2299	81	14.6	4.2	0.745	Fetal Distress
N27	2594	97	23.2	6.2	0.765	Fetal Distress
FGR 20	898	64	46.9	19.9	0.231	Fetal Distress

Table 6. SI, AMo, LTV, and STV values for fuzzy input descriptors, fuzzy assessment, and clinic diagnosis.

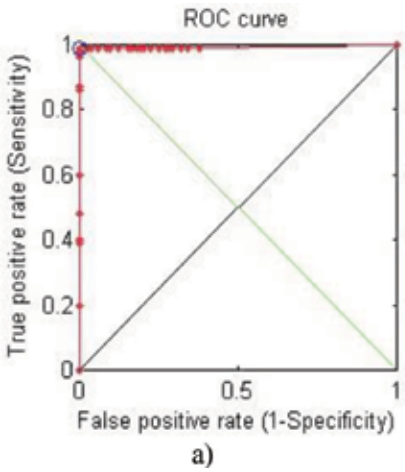

a)

True Positives	False Positives
84	0
False Negatives	True Negatives
1	103

b)

Figure 9. (a) ROC curve of the overall fuzzy system evaluation and (b) confusion matrix for 188 data evaluated.

diagnosed correctly (true negatives) by the fuzzy system. The global sensitivity was 0.9882 and global specificity was 1.

Finally, fuzzy inference system was evaluated with 21 new records of 30 minutes, classified as distress: D1-D3, and normal pregnancy: N1-N18. Each record was sampled at 2-minute interval. **Figure 10** shows the fuzzy evaluation of three records of patients with emergency

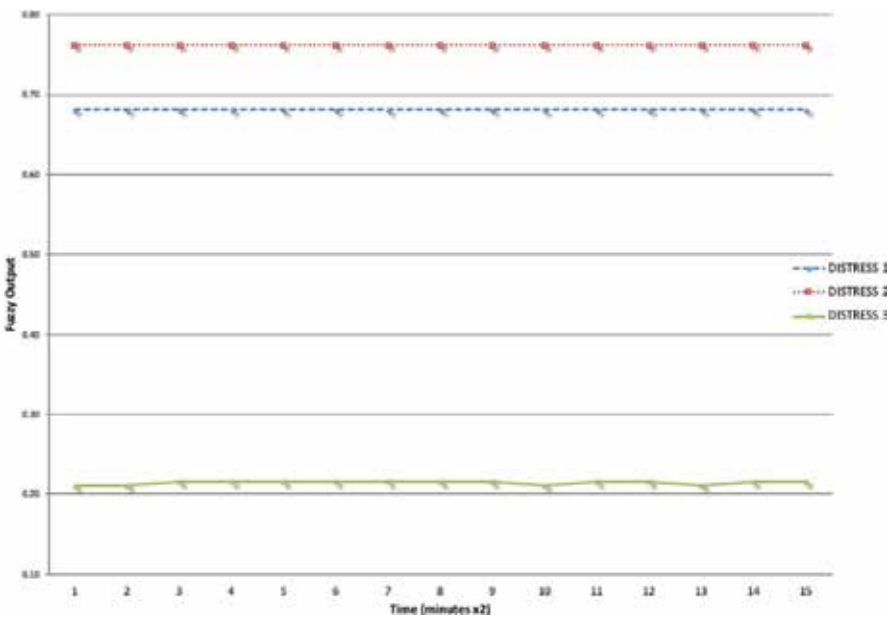

Figure 10. Fuzzy evaluation of three 30-minutes records of patients with emergency pregnancy.

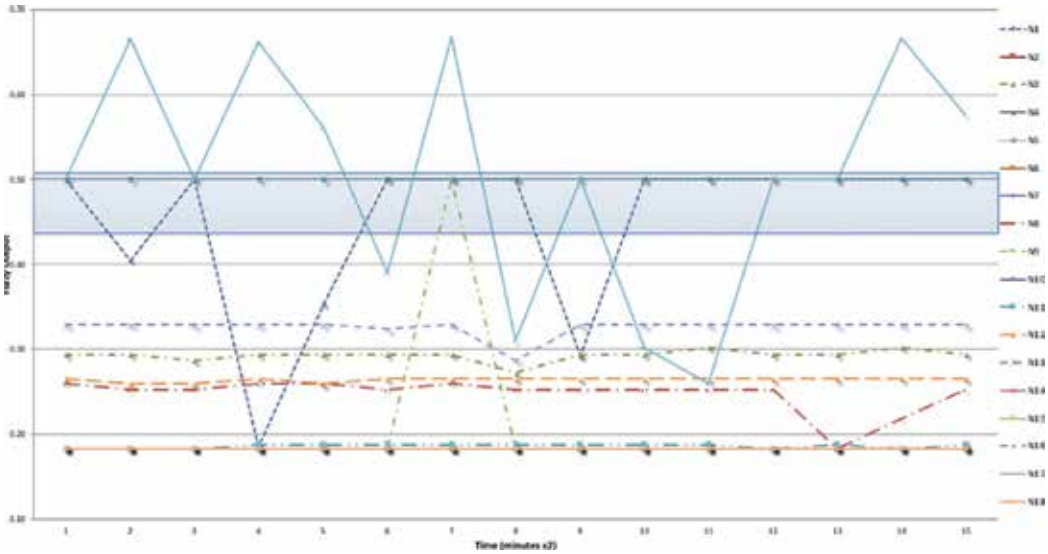

Figure 11. Fuzzy evaluation of eighteen 30-minute records of patients with normal pregnancy.

pregnancy. D1 and D2 were classified with fetal distress correctly, but D3 is shown with a normal fetal well-being state.

Figure 11 shows the fuzzy inference of 18 patients with normal pregnancy. Records N2-N4, N6-N16, and N18 show a normal fetal well-being during the 30-minute recording. The record N1 shows an indeterminate state, except for periods of 3–5 and 8–10 minutes, where the assessment of fetal well-being is normal. The record N5 was classified by the fuzzy system as indeterminate. N17 shows fetal distress from minutes 3 to 9, between minutes 15 and 21 the fetal state changes to normal, returning to distress after minute 27.

5. Conclusions

A combination of fetal HRV and CTG descriptors was proposed for discrimination between fetuses with loss of fetal well-being and normal fetuses, both in pregnancies with intrauterine growth restriction and healthy pregnancies.

The feasibility of the selected descriptors, SI, AMo, STV, and LTV was evaluated by sensitivity, specificity, and Spearman's correlation analysis, so that these parameters can be considered as evident markers of fetal well-being status in the case of FGR.

Since SI and AMo are relevant to the sympathetic part of the autonomic regulation, the opinion on the involvement of the sympathetic mechanisms in fetal distress is supported [1]. The predictive value of the parasympathetic regulation variables was lower. The growing activity of this division of the autonomic function is a marker of fetal neurological maturation [5]. The relation found between maternal and fetal HRV parameters was a sign of fetal and maternal

coupling in healthy pregnancy. Maternal respiratory sinus arrhythmia was speculated as a reason of this regularity. It was disturbed in preeclampsia [11]. Fetal growth is known to be impacted by maternal organism [6, 13]. The investigation of the possible relations between maternal and fetal HRV and its fractal components will create a novel concept of the management of women with growth-restricted fetuses.

Formerly, the most sensitive and specific for fetal distress T/QRS ratio obtained from fetal noninvasive ECG tracing was found [1, 12]. Since peaks and intervals are detectable on fetal-averaged PQRST complex, the subsequent investigation of their clinical significance is of great prospect. But the study population of the abovementioned research was suffered from preeclampsia. Thus, preeclampsia could change fetal cardiac conductivity. But will T/QRS ratio be of use in diagnosing fetal distress among all pregnant women is still a question?

The main criterion of fetal well-being is a reactivity to its motile activity by accelerating the heart rate during nonstress test [2, 3]. The obtained results could make it possible to think that SI and AMo will become an alternative to the Dawes-Redman criteria. The assessment of short-term variations (STV) and long-term variations (LTV) was found to be of use in diagnosing fetal compromise. These variables used in CTG monitors are known as the most evident markers of fetal distress [4, 9]. But the duration of the recording should be not less than 1 hour or, at least, 30 minutes. This time interval is known to be associated with better sleep/awake fetal status ratio [2, 4]. Therefore, the application of the proposed fetal HRV variables will help to use fetal noninvasive ECG tracing of the only 10 minutes long. It will be more convenient in clinical practice. Another advantage is the possibility to support or neglect fetal distress in case of negative (areactive) or false-negative nonstress test.

The hypothesis of the intrauterine programming of the diseases determines that any abnormalities during fetal life will have a subsequent clinical manifestation afterward. The cardiac signals proceeding is a convenient approach to the assessment of fetal autonomic maturation [6, 13]. Fetal HRV variables are disturbed in growth-restricted fetuses. Therefore, the investigation of fetal neurobehavioral response in case of intrauterine growth restriction is a possible way for the fetal well-being screening. But fetal growth restriction is not always associated with fetal distress and still stimulating obstetrical aggression in its projections on the term and the mode of delivery. That is why the outcome of our research in future is an advanced protocol of management of pregnant women with fetal growth restriction.

The findings of this work are based on fetal noninvasive ECG investigation. This method is still a challenge for the clinician [9]. The main problem is a low signal-to-noise ratio [1]. But fetal noninvasive ECG could be used for fetal Holter monitoring. The possibility for the creation of the system for fetal wireless distant monitoring will contribute to the better diagnosing of fetal compromise and cardiac arrhythmias.

HRV and CTG proposed descriptors can be used in an assessment system, for discrimination or prediction between fetuses with loss of fetal well-being and normal fetuses, both in pregnancies with intrauterine growth restriction and pregnancies of healthy fetuses.

Finally, a system based on fuzzy logic was designed with these descriptors in order to obtain an evaluation of the fetal well-being status. Only one false negative was obtained in the

diagnosis using 188 data, which represents an accuracy of 98.8% in fetal distress prediction, and 100% in healthy pregnancy.

Author details

Igor V. Lakhno[1], Bertha Patricia Guzmán-Velázquez[1,2]* and José Alejandro Díaz-Méndez[1,2]

*Address all correspondence to: pguzman@inaoep.mx

1 Obstetrics and Gynecology Department of Kharkiv Medical Academy of Postgraduate Education, Kharkiv, Ukraine

2 Electronics Department of National Institute of Astrophysics, Optics and Electronics, Puebla, México

References

[1] Lakhno I. The Use of Fetal Noninvasive Electrocardiography. Hindawi: Scientifica; 2016: 1-6. https://doi.org/10.1155/2016/5386595

[2] Visser et al. Cardiotocography alone is outdated and ST analysis is the way forward in fetal monitoring: FOR: Does the use of ST analysis in conjunction with cardiotocography improve perinatal outcome and/or reduce interventions for fetal distress? BJOG: An International Journal of Obstetrics and Gynaecology. 2016;**123**:1636

[3] Gupta M, Gupta P. Role of cardiotocography in high risk pregnancy and its correlation with increase cesarean section rate. International Journal of Reproduction, Contraception, Obstetrics and Gynecology. 2016;**6**(1):168-171

[4] Clark SL et al. The limits of electronic fetal heart rate monitoring in the prevention of neonatal metabolic acidemia. American Journal of Obstetrics and Gynecology. 2017;**216**(2): 163.e1-163.e6

[5] Ortiz MR, Echeverría JC, Álvarez-Ramírez J, Martínez A, Peña MA, García MT, et al. Effects of fetal respiratory movements on the short-term fractal properties of heart rate variability. Medical & Biological Engineering & Computing. 2013;**51**(4):441-448

[6] Aziz W, Schlindwein FS, Wailoo M, Biala T, Rocha FC. Heart rate variability analysis of normal and growth restricted children. Clinical Autonomic Research. 2012;**22**(2):91-97

[7] Schobel HP, Fischer T, Heuszer K, Geiger H, Schmieder RE. Preeclampsia—A state of sympathetic overactivity. New England Journal of Medicine. 1996;**335**(20):1480-1485

[8] Rosser ML, Katz NT. Preeclampsia: An obstetrician's perspective. Advances in Chronic Kidney Disease. 2013;**20**(3):287-296

[9] Reinhard J, Hayes-Gill BR, Yi Q, Hatzmann H, Schiermeier S. Comparison of non-invasive fetal electrocardiogram to Doppler cardiotocogram during the 1st stage of labor. Journal of Perinatal Medicine. 2010;**38**(2):179-185

[10] Oudijk MA, Kwee A, Visser GH, Blad S, Meijboom EJ, Rosén KG. The effects of intrapartum hypoxia on the fetal QT interval. BJOG: An International Journal of Obstetrics & Gynaecology. 2004;**111**(7):656-660

[11] Lakhno I. Autonomic imbalance captures maternal and fetal circulatory response to pre-eclampsia. Clinical Hypertension. 2017;**23**(1):5

[12] Lakhno I. Fetal non-invasive electrocardiography contributes to better diagnostics of fetal distress: A cross-sectional study among patients with pre-eclampsia. Annals of the Academy of Medicine, Singapore. 2015;**44**(11):519-523.15

[13] Ferrario M, Signorini MG, Magenes G. Complexity analysis of the fetal heart rate variability: Early identification of severe intrauterine growth-restricted fetuses. Medical & Biological Engineering & Computing. 2009;**47**(9):911-919

[14] Lakhno IV. The hemodynamic repercussions of the autonomic modulations in growth-restricted fetuses. Alexandria Journal of Medicine. 2017;**53**(4):333-336

[15] Lakhno I. The relationship between fetal and maternal hemodynamic oscillations in normal and growth restricted fetuses. Athens Journal of Health. March 2017;**4**(1):51-59

[16] Lakhno IV. A novel trophotropic mechanism of fetal wellbeing. New Armenian Medical Journal. 2014;**8**(1):68-72

[17] Liu C, Li P. Systematic methods for fetal electrocardiographic analysis: Determining the fetal heart rate, RR interval and QT interval. In: Computing in Cardiology Conference (CinC). IEEE; 2013. pp. 309-312

[18] Fuentealba P, Illanes A, Ortmeier F. Progressive fetal distress estimation by characterization of fetal heart rate decelerations response based on signal variability in cardiotocographic recordings. Computing. 2017;**44**:1

[19] Warmerdam GJ, Vullings R, Van Laar JO, Bergmans JWM, Schmitt L, Oei SG. Selective heart rate variability analysis to account for uterine activity during labor and improve classification of fetal distress. In: Engineering in Medicine and Biology Society (EMBC), 2016 IEEE 38th Annual International Conference of the IEEE. USA; 2016 August. pp. 2950-2953

[20] Fanelli A, Magenes G, Campanile M, Signorini MG. Quantitative assessment of fetal well-being through CTG recordings: A new parameter based on phase-rectified signal average. IEEE Journal of Biomedical and Health Informatics. 2013;**17**(5):959-966

Section 3

Biomedical Images Analysis

Chapter 3

Spatiotemporal Statistical Shape Model Construction for the Observation of Temporal Change in Human Brain Shape

Saadia Binte Alam and Syoji Kobashi

Additional information is available at the end of the chapter

http://dx.doi.org/10.5772/intechopen.80592

Abstract

This chapter introduces a spatiotemporal statistical shape model (stSSM) using brain MR image which will represent not only the statistical variability of shape but also a temporal change of the statistical variance with time. The proposed method applies expectation-maximization (EM)-based weighted principal component analysis (WPCA) using a temporal weight function, where E-step estimates Eigenvalues of every data using temporal Eigenvectors, and M-step updates Eigenvectors to maximize the variance. The method constructs stSSM whose Eigenvectors change with time. By assigning a predefined weight parameter for each subject according to subjects' age, it calculates the weighted variance for time-specific stSSM. To validate the method, this study employed 105 adult subjects (age: 30–84 years old with mean ± SD = 60.61 ± 16.97) from OASIS database. stSSM constructed for time point 40–80 with a step of 2. The proposed method allows the characterization of typical deformation patterns and subject-specific shape changes in repeated time-series observations of several subjects where the modeling performance was observed by optimizing variance.

Keywords: stSSM, brain, MRI, shape analysis, age, prediction

1. Introduction

Quantifying cortical morphological dynamics of brain deformation will help neuroscientists identifying and characterizing brain deformation disorders. To be precise, if physicians could learn to predict the normal cortical shape evolution for healthy adults, they can predict

abnormal or early deformation of brain with time as well. The shape variability from statistical shape models has been successfully utilized to perform various deformation-based researches in the field of image analysis in both two-dimensional (2D) and three-dimensional (3D) images. In specific cases, their application for image segmentation in the context of statistical shape models has been well acknowledged. To constract those statistical models, a set of segmentations of the shape of interest is required. At the same time, a set of feature vectors are also needed which can be decidedly defined in each sample shape. There are a number of researchers who have used statistical models containing shape information as initials for segmentation via deformable models [1–3], deformable registration [4], or shape analysis [5]. Meanwhile, the fundamental problem faced at the time of constructing these models is the reality that they need the determination of point correspondences between the different shapes as the manual identification of such correspondences is a time-consuming and tiresome work. It is specially applicable in 3D where the number of feature vectors required to describe the shape accurately rises dramatically compared to 2D applications. An easy but efficient way of handling this issue for the construction of statistical shape models is the use of distance transformations which has been proposed by a number of authors [2, 6, 7]. For example, in [2], the authors proposed an approach in which the statistical analysis is carried out directly on the signed distance maps of a set of aligned shapes.

However, learning predictive models to trace forth the evolution trajectories of adult cortical shapes remains challenging. There are some studies to analyze the brain deformation in adults. For example, they are studying nonrigid brain shape registration with respect to baseline distribution, brain region segmentation based on fuzzy object model, sulcal curves extraction on the outer cortex, etc. In [8], authors described an automated way in which correspondences between the surfaces of different shapes are established via a nonrigid registration algorithm [9]. A similar approach has been proposed by [10]: there, a modified iterative closest point algorithm [11] is used to calculate correspondences between geometric surface features of the shapes such as crest lines. The difficulty of analyzing the adult brain shape points to the critical selection of parameter optimization.

Recently, Durrleman et al. [12] have proposed the construction method of spatiotemporal statistical shape model but the study is confined to longitudinal data. To fill this critical gap, we propose spatiotemporal statistical shape model (stSSM) for temporal 3D shape change analysis of the adult brain. We are performing a dimensionality reduction analysis directly on a parametric representation of the feature vector calculated from training sample. To match different anatomies, all subjects are aligned using anterior-commissure (AC), posterior-commissure (PC), and mid-plane for location and orientation alignment with a reference of AC as origin. This enables the construction of average models of the brain shape and their statistical variability across a population of subjects. Our approach is closely related to the statistical shape models first proposed by [13, 14], but differs in an important aspect. Rather than performing a classic principal component analysis (PCA) directly, we are creating an stSSM for temporal 3D shape change analysis of the adult brain with respect to cortical surfaces using an expectation-maximization (EM)-based weighted PCA (WPCA) learning framework where the weight function is defined as a Gaussian function, whose center is time point, and variance is a predefined parameter.

http://dx.doi.org/10.5772/intechopen.80592

2. Preliminary

Basically, SSM construction is a method of extracting the average shape and a number of modes of variation from a collection of training samples. The methods are strongly dependent on the chosen shape of representation. A vital necessity for building shape models with statistical variability is that the features of all training samples need to be located at corresponding positions and sharing same origin. With an assumption of a one-to-one correspondence of anatomical structures across subjects, the alignment of images between different subjects with chamfer distance calculation provides a dense set of correspondences. In this study, we performed an expectation-maximization algorithm-based wPCA on a compact parameterization of the feature vector which is required to construct our proposed model. In the following subsections, we will describe the proposed approach in detail.

2.1. Distance mask calculation

For distance mask calculation, level sets were introduced by [15] and made popular for computer vision and image analysis by [16]. They basically feature an implicit shape representation and can be utilized with regional or edge-based features. The authors of [17] presented a method of embedding the distance maps into the linear space, which could solve the modeling problems and Cremers et al. [18] have given an overview of statistical approaches to level set segmentation including prior shape knowledge.

In order to construct stSSM, firstly, brain region was segmented from MR images. The segmentation is done automatically using FSL [19]. In the next step, chamfer distances were calculated to extract shape features through a level set algorithm where negative values are assigned inside the brain region and positive value outside the brain region.

2.2. Dimensionality reduction

After calculation of chamfer distance, the next step is to reduce the dimensionality of the training set, that is, to find a small set of modes that best describes the observed variation. This is usually accomplished using principal component analysis (PCA) [20]. PCA is a very powerful tool to analyze data by creating a custom set of "principal component" eigenvectors that are optimized to describe the most data variance with the fewest number of components. Theoretically, the steps are simple: the principal components $\{\boldsymbol{\Phi}_k\}$ of a dataset are simply the eigenvectors of the covariance of that dataset, sorted by their descending eigenvalues which results to a new observation, $\boldsymbol{C} = \boldsymbol{\mu} + \sum \psi_k \boldsymbol{\Phi}_k$ where $\boldsymbol{\mu}$ is the mean of the initial dataset and ψ_i is the reconstruction coefficient for eigenvector $\boldsymbol{\Phi}_i$ [21]. One of the limitation of classic PCA is that it does not distinguish between variance due to measurement noise *vs*. variance due to genuine underlying signal variations. Even when an estimation of the measurement variance is available, this information is not included while constructing the eigenvectors [22]. In order to overcome this problem, Bailey [22] introduces PCA based on EM-PCA.

In our method, we used weighted PCA with EM-PCA. EM is an iterative technique for solving parameters to maximize a likelihood function for models with unknown latent variables

which basically consists of E-step and M-step. E-step estimates eigenvalues of every data using temporal eigenvectors, and M-step updates eigenvectors so that it maximizes the variance. E- and M-steps are iterated until convergence of updating vectors. The detail is described below.

[E-step] Let the current eigenvector be $\vec{\Phi}$. Principal component (PC) score of data j is calculated by:

$$c_j = \vec{x}_j \cdot \vec{\Phi} \tag{1}$$

where $\vec{x}_j$ is the feature vector of data j.

[M-Step] Update the eigenvector by maximizing the weighted variance of PC score. It is calculated by:

$$\vec{\Phi} = \sum_j w_j c_j \vec{x}_j \tag{2}$$

The eigenvectors are normalized after each M-step. E- and M-steps are iterated till the updated value of eigenvector is converged.

3. Method

To construct stSSM, firstly, brain region was segmented from MR images, and chamfer distances were calculated to extract shape features as shown in **Figure 1**.

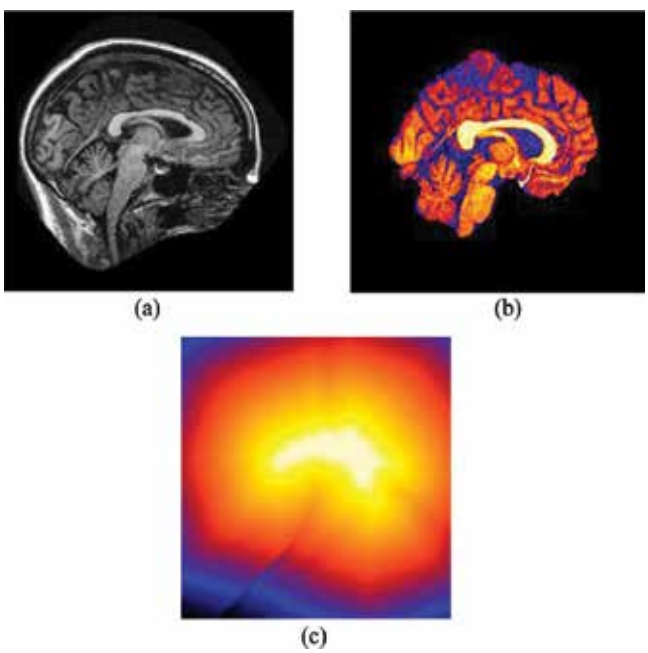

Figure 1. Preprocessing steps of brain MR image for feature extraction. (a) Raw MR image, (b) Segmented image, and (c) Signed distance.

http://dx.doi.org/10.5772/intechopen.80592

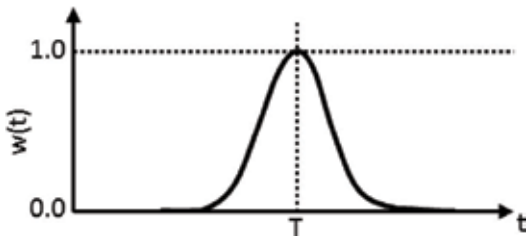

Figure 2. Temporal weight function.

After that, weighted PCA is applied to the shape features. The proposed method assigns a weight parameter for each subject according to subjects' age, and calculates the weighted variance. Let t_i be a time point, and the method can construct SSM at the time point. The weight function was defined as a Gaussian function, whose center is t_i, and variance is a predefined parameter.

$$w_j = \exp\left(-\frac{(t-t_j)^2}{\sigma^2}\right) \tag{3}$$

The shape of temporal weight function is illustrated in **Figure 2**. That is, subjects near t_i are dominant to decide the Eigenvectors. By shifting the t_i at a short interval from the minimum to the maximum age, the method constructs the stSSM whose eigenvectors change with growing or aging. Preliminarily, the eigenvector at the first time point is initialized randomly. Then, the obtained eigenvectors are used at the stSSM construction.

4. Experimental results

For evaluation purpose, the proposed method has been applied on both artificial and image data.

4.1. Result of artificial data

In order to numerically evaluate the method, weighted PCA has been applied to point distribution model. Assumed a point of an organ, and the statistical distribution changes temporally. **Figure 3** shows the artificially generated 2D data where the points located one direction shown at the first time point (a), and rotates anticlockwise with 10-degree every time point. The time period was 20. Because, conventional SSM evaluates all data simultaneously without time, as shown in **Figure 3(c)**. It cannot be statistical variation of shape.

Figure 4 shows the angle between x-axis and the first (second) principal axis obtained by the proposed method. The full-width-half-maximum (FWHM) of the weight Gaussian function was 3. The first principal axis rotates anticlockwise with 10-degree every time point. Results show that the proposed method can extract the statistical variability of point distribution in time. Note that the result around t = 1 has errors because the data existed only in the positive side of Gaussian function.

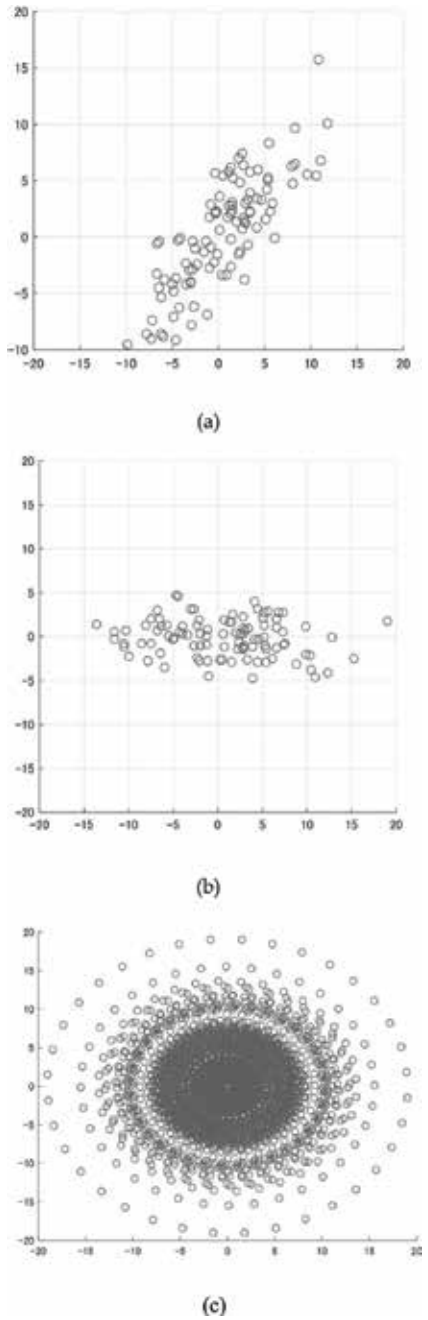

Figure 3. Temporal change point distribution. (a) t = 1, (b) t = 5, and (c) all data.

4.2. Image data

To train and test the proposed model with respect to weighted variance optimization, we used 105 adult subjects (age: 30–84 years old with mean ± SD = 60.61 ± 16.97) from publicly

http://dx.doi.org/10.5772/intechopen.80592

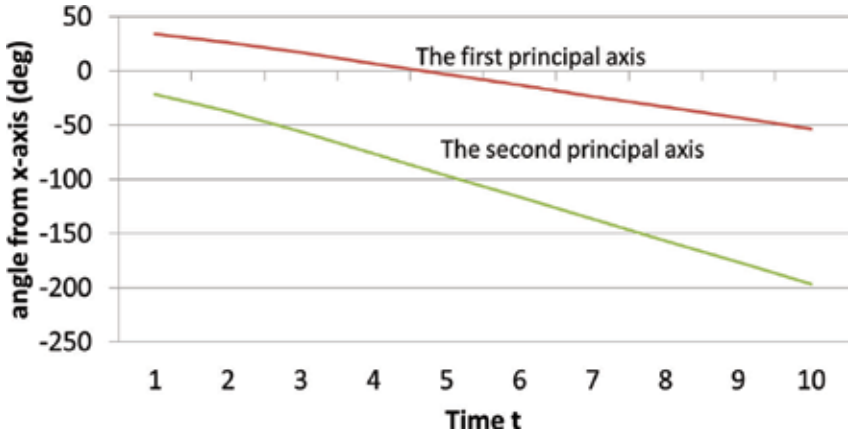

Figure 4. Temporal change of principal axes.

available imaging database called OASIS [23]. These subjects were selected from a larger database of individuals who had participated in MRI studies at Washington University, were all right-handed, and older adults had a recent clinical evaluation. The representative MR imaging acquisition parameters were repetition time (TR) of 9.7 ms, echo time (TE) of 4.0 ms, image resolution (voxel) of 256 by 256, flip angle (FA) of 10°.

4.3. Results

The method was applied to the adult brain MR image. We first segmented the brain region from MR images, and calculated the signed distance map to extract shape features. The proposed method assigns a weight parameter for each subject according to subjects' age, and calculates the weighted variance. Let t_i be a time point, and the method can construct SSM at the time point. According to the weight function defined in Eq. (3), the center is t_i, and variance is a predefined parameter.

From **Figure 2**, we can understand the shape of temporal weight function which implies that subjects near t_i are dominant to decide the Eigenvectors. By shifting the t_i at a short interval from the minimum to the maximum age, the method constructs the stSSM whose eigenvectors change with aging. Preliminarily, the eigenvector at the first time point is initialized randomly (usual PCA can be applied to obtain the initial eigenvector). Then, the obtained eigenvectors are used at the following stSSM construction. **Figure 5** shows the mean shape of constructed model between age range of 40–80 years old. **Figure 6** illustrates stSSM of brain of adult subject at 60 years. The brain shape changes along with temporal domain with reference to variance (σ) can be seen.

Next, the stSSM of adult brain between 52 and 58 years and temporal difference with changing variance is shown in **Figure 7**. While generating stSSM for an age range of 40–80, Gaussian function's weight parameter has been varied between a range of 5–35.

Figure 8 illustrates stSSM of adult subject brain shape at age of 60 years old, where the individual brain shape variety is synthesized within a range of −1σ to +1σ at the first eigenvector

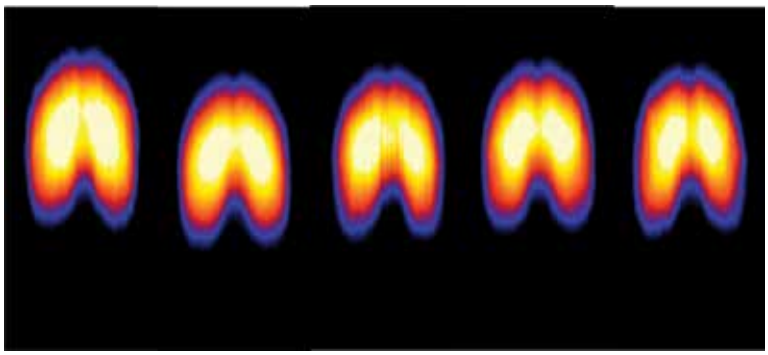

Figure 5. stSSM mean shape (a) 40 years (b) 50 years (c) 60 years (d) 70 years, and (e) 80 years.

(horizontal) and −0.5σ to +0.5σ at the second eigenvector (vertical) with a step of 0.50. σ is the standard deviation (SD) in the training data along each eigenvector. Full-width-half-maximum (FWHM) of the Gaussian weight function used in this case was 15.

5. Discussion

The 3D SSM and stSSM in the medical imaging field are almost exclusively based on imaging modalities such as CT, MRI, that is, the original data representation of the training shapes is not a mesh but rather a segmented volume. Therefore, each shape of the training set must be annotated by features, each designating the same anatomical locus along the set. The set is considered as a collection of shape vectors which after alignment raises a covariance matrix. **Figures 1** and **2** show these phases of our model from which we created feature vector matrix from 105 training samples.

For dimensionality reduction phase, we introduced weighted EM-PCA where every aligned training shape is described by the feature vector matrix. The mean shape has been formed by simply averaging over all samples with corresponding weight parameter where weight has been assigned by subject's age. From age range of 40–80 years with a step of 2, stSSM model in 3D has been constructed. An eigen decomposition on covariance matrix gives principal modes of variation (eigenvectors) and their respective variances (eigen values). **Figure 5** visualizes the mean shape of 40, 50, 60, 70, and 80 years. From the computational point of view, this method is used due to higher numerical stability. The resulting modes of variation are ordered by their variances. In a next step, the model approximated every valid shape by a linear combination of the chosen accumulated variance which presented the shape variation with FWHM Gaussian distribution function. The shape variation at a specific time point is visualized in **Figure 6**. The horizontal and vertical axes are the first and the second principal axes.

Difference between temporal deformations of all parameters has been shown in **Figure 7**. We calculated the temporal deformation change between two time points and evaluated the corresponding difference. Positive value has been assigned inside, while negative represents outside with a view that higher temporal deformation difference will show high contrast. Our

http://dx.doi.org/10.5772/intechopen.80592

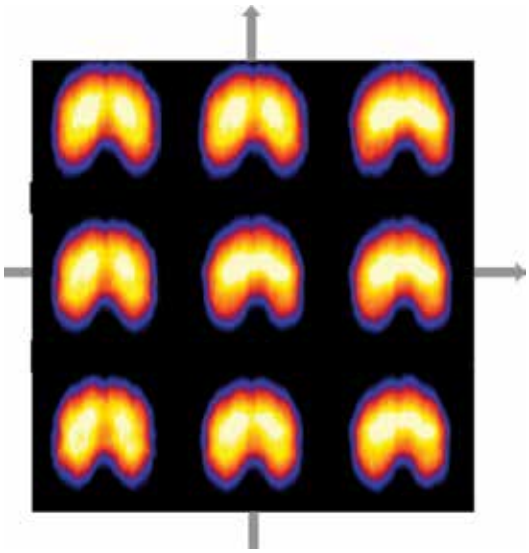

Figure 6. Spatiotemporal statistical shape model of adult brain. The horizontal and vertical axes are the first and the second principal axes.

study shows that when FWHM of Gaussian function is set to a value smaller than 15, it shows larger difference in comparison with FWHM higher than 15 where it is not represented. This observation leads to an optimum value of weight parameter between 10 and 15. Constructed stSSM for specific age is shown in **Figure 8**.

The proposed method was evaluated by generalization ability according to leave-one-out cross validation (LOOCV) procedure. Generalization ability evaluates the performance of representing

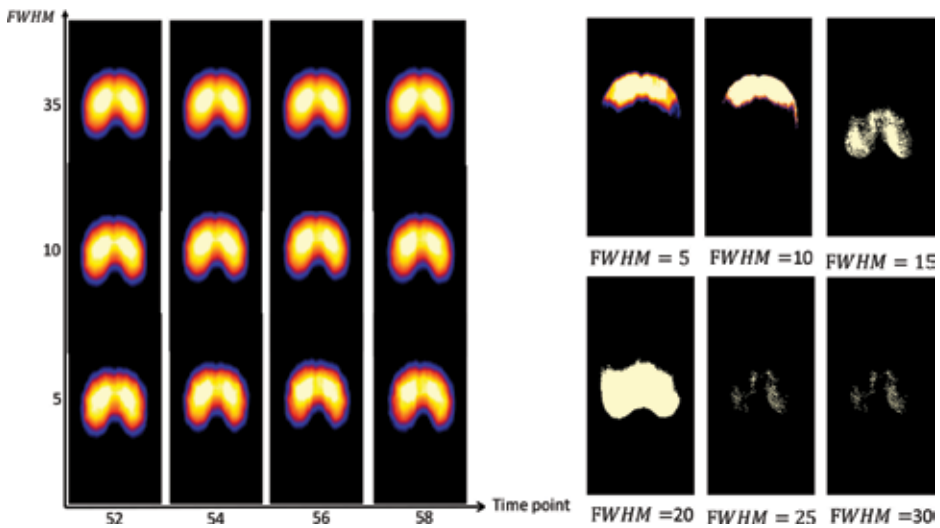

Figure 7. Temporal difference with changing variance.

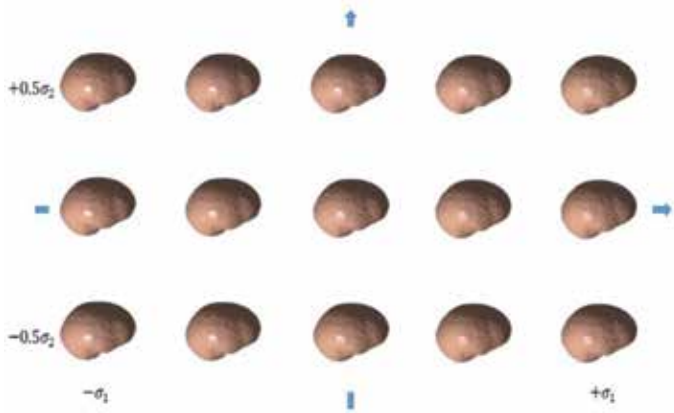

Figure 8. Spatiotemporal statistical shape model of adult brain. The horizontal and vertical axes are the first and the second eigenvectors. The individual brain shape variety is synthesized within a range of −1σ to +1σ at the first eigenvector (horizontal) and −0.50σ to +0.50σ at the second eigenvector (vertical) with a step of 0.50. σ is the standard deviation in the training data along each eigenvector.

new acceptable models. First, data of the evaluation subject were projected into stSSM of the evaluation subject's age. Next, brain shape of evaluation data was reconstructed, and compared with the original data. Evaluation criteria used in this study was Jaccard Index (J.I.). To restrict the allowed variation to plausible shapes, weight parameter is assigned to a certain interval. Mean ± standard deviation of generalization ability with different Gaussian distribution function has also calculated. Overall, FWHM value 15 achieves the best prediction result which closely follows observation-based optimum value of weight parameter between 10 and 15.

6. Conclusion

Nowadays, statistical shape models have become an exciting robust tool for shape representation of medical images. The use of both 2D and 3D models appeared into the scenario in recent years. In this chapter, we introduced a 3D stSSM for brain MRI data. The presented method allows the characterization of typical deformation patterns and subject-specific shape changes in repeated time-series observations of several subjects. The modeling performance was observed by optimizing variance. This study can be seen as an extension of the usual statistical shape model of scalar measurements to high-dimensional shape or image data. From the analysis of difference between all parameters of temporal deformation, we can draw a conclusion toward optimum value of FWHM.

We believe that the discussed method of this chapter enables the automatic construction of statistical models in 3D and is not limited to the brain but can be applied to other anatomical structures such as the heart or liver. The spatiotemporal statistical shape model has a wide number of possible applications primarily in segmentation and morphometry. Another potential application of this method lies in the use of statistical modes of variation as a priori knowledge for image registration. We are currently working on this idea which uses the modes of variation from predefined weight parameter to provide a more

compact parameterization of stSSMs. This may be specifically useful for intersubject analysis tasks where these modes of variation can be learnt from a sample population of subjects as shown in this chapter.

Another potential scope is the morphometric comparison of differences between groups of subjects. Currently available morphometric methods can be classified into voxel-based [24, 25] or deformation-based methods [26, 27]. Mostly, voxel-based methods depend on a global registration between subjects followed by a statistical analysis of tissue differences to differentiate between groups of subjects. On the other hand, deformation-based methods use the information encoded in the deformation to describe the anatomical variability between groups. Future work will include investigation whether statistical shape models can be used as a deformation-based morphometric tool to characterize shape differences between groups of normal and AD subjects.

Ethical approval

All applicable international, national, and/or institutional guidelines for the care and use of animals were followed. This study does not contain uninformed patient data.

Acknowledgements

This work was supported in part by JSPS Grant-in-Aid for Scientific Research on Innovative Areas (Multidisciplinary Computational Anatomy) JSPS KAKENHI Grant Number 17H05304.

Conflict of interest

The authors of this chapter declare that they have no conflict of interest.

Author details

Saadia Binte Alam* and Syoji Kobashi

*Address all correspondence to: saadiabinte@iee.org and kobashi@eng.u-hyogo.ac.jp

Graduate School of Engineering, University of Hyogo, Japan

References

[1] Kelemen A, Székely G, Gerig G. Elastic model-based segmentation of 3-D neurological data sets. IEEE Transactions on Medical Imaging. 1999;**18**:828-839

[2] Leventon ME, Grimson WEL, Faugeras O. Statistical shape influence in geodesic active contours. In: Proceedings of Conference on Computer Vision Pattern Recognition. 2000. pp. 316-323

[3] Cremers D, Schnörr C, Weickert J. Diffusion-snakes combining statistical shape knowledge and image information in a variational framework. In: Proceedings on IEEE Workshop Variational Level Set Methods. 2001. pp. 137-144

[4] Wang Y, Staib LH. Elastic model based nonrigid registration incorporating statistical shape information. In: Proceedings of 1st Conference on Medical Image Computing and Computer-Assisted Intervention (MICCAI'98). 1998. pp. 1162-1173

[5] Styner M, Gerig G. Medical models incorporating object variability for 3-D shape analysis. In: Proceedings of 17th International Conference on Information Processing Medical Imaging. 2001. pp. 502-516

[6] Golland P, Grimson WEL, Shenton ME, Kikinis R. Small sample size learning for shape analysis of anatomical structures. In: Proceedings of 3rd International Conference on Medical Image Computing Computer-Assisted Intervention. 2000. pp. 72-82

[7] Davis CA. Deformation analysis for shape based classification. In: Proceedings of 17th International Conference on Information Processing Medical Imaging. 2001. pp. 517-530

[8] Frangi AF, Rueckert D, Schnabel JA, Niessen WJ. Automatic construction of multiple-object three-dimensional statistical shape models: Application to cardiac modeling. IEEE Transactions on Medical Imaging. 2002;**21**:1151-1166

[9] Rueckert D, Sonoda LI, Hayes C, Hill DLG, Leach MO, Hawkes DJ. Non-rigid registration using free-form deformations: Application to breast MR images. IEEE Transactions on Medical Imaging. 1999;**18**:712-721

[10] Subsol G, Thirion JP, Ayache N. A scheme for automatically building three-dimensional morphometric anatomical atlases: Application to a skull atlas. Medical Image Analysis. 1998;**2**(1):37-60

[11] Besl PJ, McKay ND. A method for registration of 3-D shapes. IEEE Transactions on Pattern Analysis and Machine Intelligence. 1992;**14**:239-256

[12] Durrleman S, Pennec X, Trouvé A, Braga J, Gerig G, Ayache N. Toward a comprehensive framework for the spatiotemporal statistical analysis of longitudinal shape data. International Journal of Computer Vision. 2013;**103**(1):22-59

[13] Joshi SC. Large Deformation Diffeomorphisms and Gaussian Random Fields for Statistical Characterization of Brain Sub-Manifolds [Ph.D.]. St. Louis, MO: Department of Electrical and Systems Engineering, Washington Univ.; 1998

[14] Gee JC, Bajcsy RK. Elastic matching: Continuum mechnanical and probabilistic analysis. In: Brain Warping. 1998;**2**:183-197

[15] Osher S, Sethian JA. Fronts propagating with curvature-dependent speed: Algorithms based on Hamilton–Jacobi formulation. Journal of Computational Physics. 1988; **79**(1):12-49

[16] Malladi R, Sethian J, Vemuri B. Shape modeling with front propagation: A level set approach. IEEE Transactions on Pattern Analysis and Machine Intelligence. 1995; **17**(2):158-174

[17] Pohl KM, Fisher J, Shenton M, McCarley RW, Grimson WEL, Kikinis R, Wells WM. Logarithm odds maps for shape representation. In: Proceedings of International Conference on Medical Image Computing and Computer-Assisted Intervention. 2006. pp. 955-963

[18] Cremers D, Rousson M, Deriche R. A review of statistical approaches to level set segmentation: Integrating color, texture, motion and shape. International Journal of Computer Vision. 2007;**72**(2):195-215

[19] Andersson JLR, Jenkinson M, Smith S. Non-Linear Registration, Aka Spatial Normalisation, FMRIB Technical Report TR07JA22007. pp. 1-21

[20] Heimann T, Meinzer HP. Statistical shape models for 3D medical image segmentation: A review. Medical Image Analysis. 2009;**19**(4):543-563

[21] Alam SB, Nakano R, Kobashi S. Brain age estimation using multiple regression analysis in brain MR image. International Journal of Innovative Computing, Information and Control. 2016;**12**(4):1385-1396

[22] Bailey S. Principal component analysis with noisy and/or missing data. Astronomical Society of the Pacific. 2012;**124**:919

[23] http://www.oasis-brains.org/

[24] Ashburner J, Friston KJ. Voxel-based morphometry—The methods. NeuroImage. 2000; **11**(6):805-821

[25] Bookstein FL. 'Voxel-based morphometry' should not be used with imperfectly registered images. NeuroImage. 2001;**14**(6):1452-1462

[26] Ashburner J, Hutton C, Frackowiak R, Johnsrude I, Price C, Friston K. Identifying global anatomical differences: Deformation-based morphometry. Human Brain Mapping. 1998;**6**: 638-657

[27] Chung MK, Worsley KJ, Paus T, Cherif DLCC, Giedd JN, et al. A unified statistical approach to deformation-based morphometry. NeuroImage. 2001;**14**(3):595-606

Chapter 4

Noncontact Monitoring of Vital Signs with RGB and Infrared Camera and Its Application to Screening of Potential Infection

Guanghao Sun, Toshiaki Negishi, Tetsuo Kirimoto, Takemi Matsui and Shigeto Abe

Additional information is available at the end of the chapter

http://dx.doi.org/10.5772/intechopen.80652

Abstract

In recent years, much attention is being paid to research and development of technology that provides noncontact measurement of vital signs, i.e., heart rate, respiration, and body temperature, which are important for understanding the state of a person's health. As technology for sensing biological information has progressed, new biological measurement sensors have been developed successively. There have also been reports regarding methods for measuring respiration or heart rate using pressure sensors, microwave radar, air mattresses, or high-polymer piezoelectric film. The methods have wide-ranging applications, including systems for monitoring of elderly people, identification of sleep apnea, detection of patients suspected to have an infectious disease, and noncontact measurement of stress levels. In this chapter, the principles behind noncontact measurement of respiration and heartbeat using infrared/RGB facial-image analysis are discussed, along with the applications for such measurement in the detection of patients suspected to be suffering from infectious diseases.

Keywords: vital sign, noncontact, thermal image, infection screening, respiration

1. Introduction

Much attention is being paid to research and development of technology that provide noncontact measurement of vital signs, such as heartbeat, respiration, and body temperature,

which are important for understanding the state of a person's health. In the past, a practice called "悬丝诊脉 (suspension examination)" was documented in China's Tang Dynasty, 1400 years ago. Prominent physician Sun Simiao used strings to perform pulse diagnosis from the radial artery pulse without touching the patient's body, demonstrating that minute movements on the body's surface and changes in facial coloring have been used to obtain biological information and perform diagnoses since long ago. In recent years, as technology for sensing biological information has progressed, new biological measurement sensors have been developed successively. There have also been reports regarding methods for measuring respiration or heartbeat using pressure sensors [1], microwave radar [2], air mattresses, or high-polymer piezoelectric film. The methods have wide-ranging applications, including systems for monitoring elderly people [3], identification of sleep apnea [4], detection of patients suspected to have an infectious disease [5, 6], and noncontact measurement of stress levels [7]. In this chapter, the principles behind noncontact measurement of respiration and heartbeat using infrared/RGB facial-image analysis are discussed, along with the applications for such measurement in the detection of patients suspected to be suffering from an infectious disease.

2. Principles of measuring respiratory/heart rate using infrared/RGB facial-image analysis

The blood vessels throughout the body are broadly categorized as arteries or veins, and there is a difference in the manner in which the volume of blood flowing through each blood vessel type changes. Blood flow volume through veins changes little, whereas blood flow volume through arteries varies according to the pulse. Further, one of the properties of oxygenated hemoglobin in the blood flowing through arteries is that it easily absorbs light from a specific wavelength. Because of these properties, when the skin is exposed to continuous light of a specific wavelength, the reflected light changes according to variation in blood flow volume, and the pulse waveform can be obtained by continuing to measure that reflected light [8]. The pulse wave obtained here is referred to as a volume pulse wave.

The simplicity and noninvasiveness of obtaining measurements with a photoplethysmography (PPG) sensor have led to the PPG sensor's application as a tool for monitoring health [9, 10]. In PPG sensors, light is emitted from a dedicated light source (wavelengths 660 and 940 nm), and the volume pulse wave is obtained by measuring the reflected light with photodiodes. In this study, heartbeat was measured with an RGB camera by substituting ambient light for the dedicated light source and an RGB camera for the photodiodes and then measuring the form of the volume pulse wave in the same way as in PPG. Because of the degree of skin exposure and ease of detection, the heartbeat waveform was measured from the face. Additionally, respiration was measured by using thermography to detect nasal-region temperature changes associated with respiration. During exhalation, warm air from inside the lungs is released and it increases the temperature in the nasal region, whereas during inhalation, cool air from the external environment is breathed in and it lowers the temperature in the nasal region. The respiration waveform can be obtained by using an infrared camera to

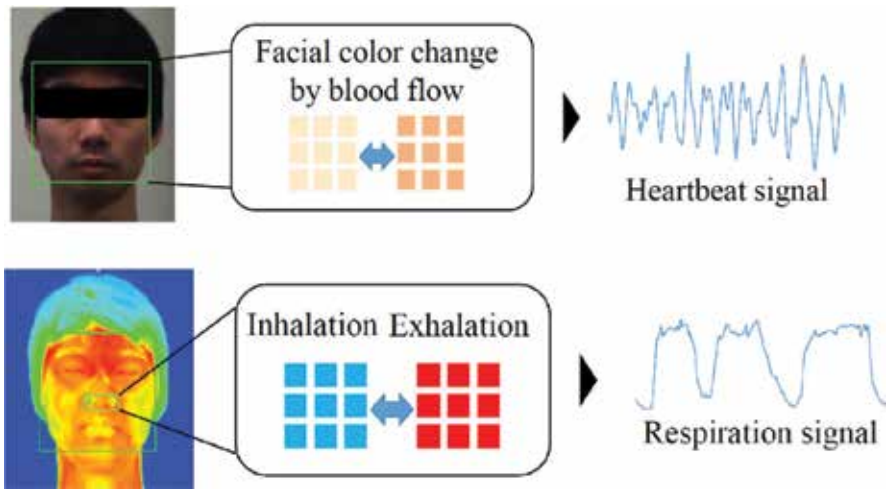

Figure 1. Principles of measuring respiratory/heart rate using infrared/RGB facial-image analysis.

measure such nasal-region temperature changes associated with respiration. **Figure 1** shows the principles of measuring respiratory/heart rate using infrared/RGB facial-image analysis.

3. Evaluation of the accuracy of measuring respiratory/heart rate using infrared/RGB facial-image analysis

3.1. Experimental protocol

The experiment was conducted with ten healthy university students. An infrared/RGB camera was set up 50 cm in front of the measurement subjects, and the subjects were instructed to sit and maintain a resting state. Images were taken for 30-s periods when at rest and after exercise (ergometer exercise: 70 rpm, 100 W, 2-min duration). Furthermore, measurements

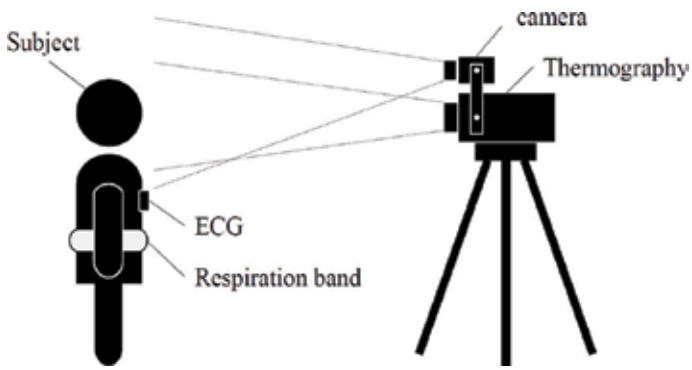

Figure 2. Experimental protocol.

were also taken simultaneously using thoracoabdominal respiration sensors and an electrocardiogram as references for respiratory rate and heart rate, respectively (**Figure 2**).

The nasal area was manually extracted from the infrared images taken (150 × 150 pixels). During respiration, the temperature of the nasal area changes as air moves in and out. These temperature changes over time were recorded to create a waveform. A band-pass filter (0.17–0.42 Hz) was applied to this waveform by a signal processer. Then, the waveform was normalized, and the autocorrelation function was calculated. Last, the respiratory rate was calculated based on the peak interval of the autocorrelation function calculated earlier. Meanwhile, the visible images taken with the RGB camera were converted to a single color (green), and an area centered on the nose (150 × 180 pixels) was extracted. The formula below was applied to the extracted image to calculate luminance value Y [11]:

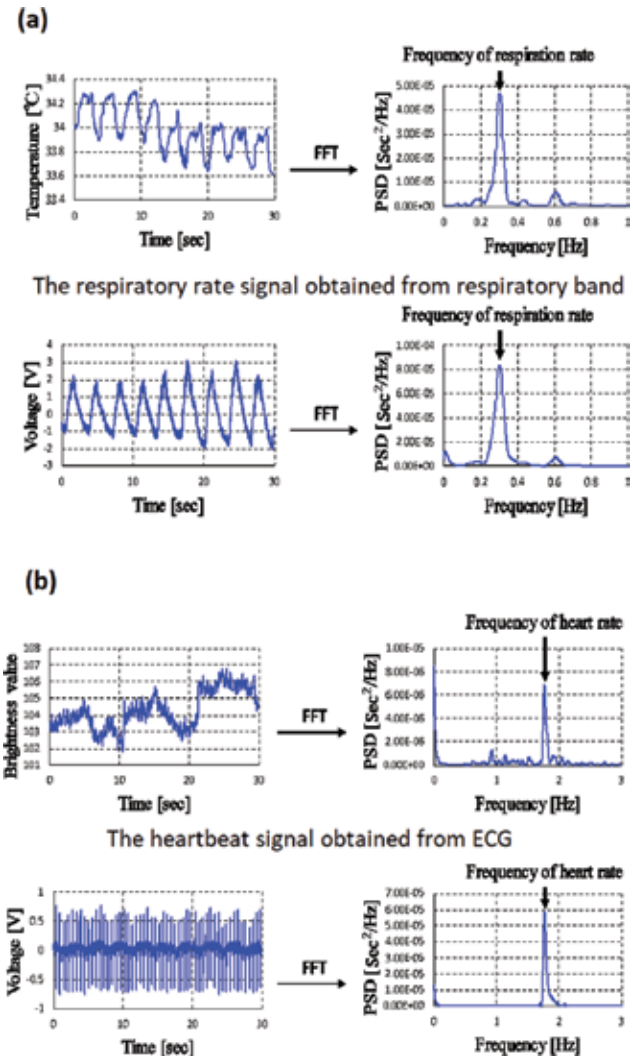

Figure 3. Respiration curves obtained from thoracoabdominal respiration sensors and infrared images; heartbeat curves obtained from ECG and visible images. (a) The respiratory rate signal obtained from IR camera. (b) The heartbeat signal obtained from RGB camera.

$$Y = (0 \;\; 0.587 \;\; 0)\begin{pmatrix} R \\ G \\ B \end{pmatrix} \tag{1}$$

The luminance values calculated were recorded over time to create a waveform. A band-pass filter (0.83–2.5 Hz) was applied to this waveform. Afterward, the same type of processing as in respiratory rate calculation was performed to calculate the heartbeat.

3.2. Results

Figure 3(a) shows the respiration-heartbeat curves obtained from the thoracoabdominal respiration sensors and infrared images. **Figure 3(b)** shows the heartbeat curves obtained from the ECG and visible images. They demonstrate that both respiration and heartbeat are similar to the curves obtained from the references.

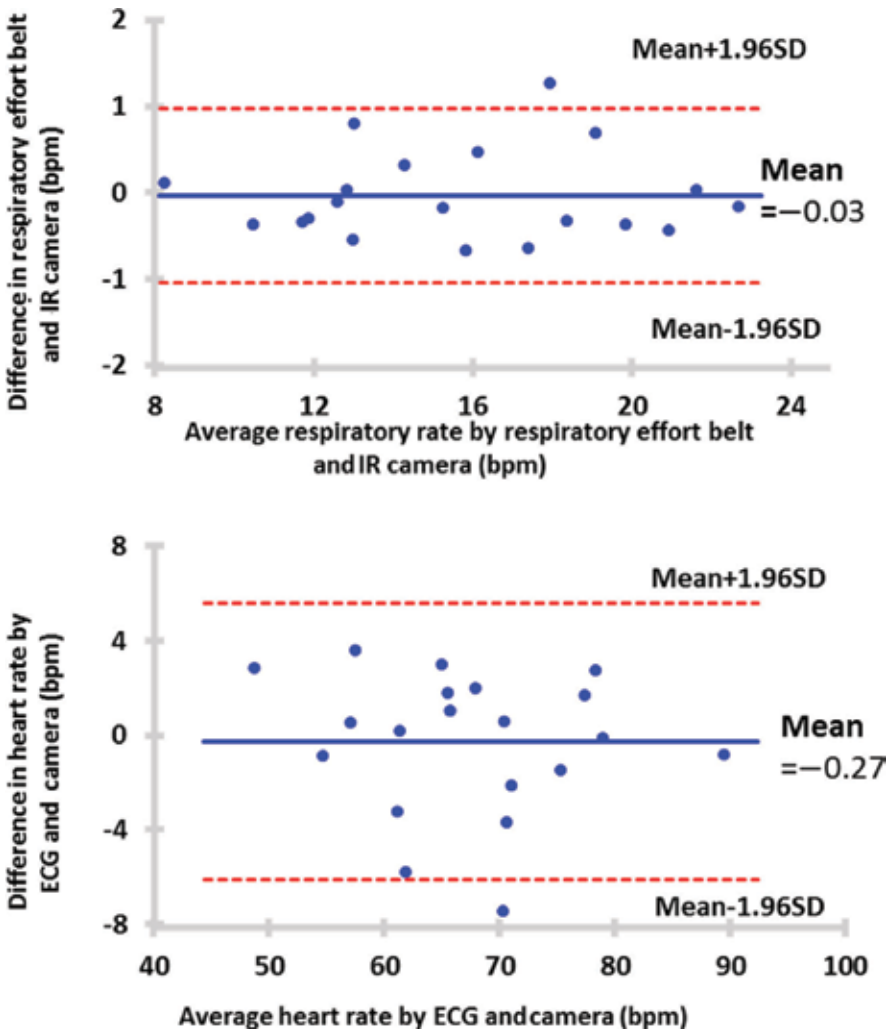

Figure 4. Plot of respiration/heart rate from Bland-Altman analysis.

Next, a Bland-Altman analysis was applied to all 20 pieces of data obtained from each subject at rest and after exercising, and the accuracy was verified (**Figure 4**). The results for respiratory rate were as follows: a correlation coefficient of 0.99 ($p < 0.01$), an average difference of −0.03 (breaths per minute) between the respiratory rates obtained from the infrared images and thoracoabdominal respiration sensors, and a 95% confidence interval of −1.04 to 0.9 (breaths per minute). The results for heart rate were as follows: a correlation coefficient of 0.96 ($p < 0.01$), an average difference of −0.27 (beats per minute) between the respiratory rates obtained from the visible images and ECG, and a 95% confidence interval of −6.1 to 5.5 (beats per minute). These results demonstrate that highly accurate measurement of respiratory rate and heart rate are possible, regardless of how those values fluctuate (respiratory rate: 9.2–23.9 breaths per minute, heart rate: 47.9–93.9 beats per minute).

4. Applications in infectious-disease screenings for respiratory/heart rate measurement technology using infrared/RGB facial-image analysis

In recent years, much importance has been placed on developing new quarantine systems to use against emerging infectious diseases and epidemics involving new strains of viruses. From past outbreaks of severe acute respiratory syndrome (SARS) to the H1N1 flu virus, a variety of infectious diseases have spread widely, causing damage to countries around the world. Although some of those infectious diseases are in the process of being eradicated, there are also fears about outbreaks of reemerging and emerging infectious diseases. In these conditions, it is essential to take preventive measures at national borders at the time when a person enters the country, and quarantine inspection at airports and the like includes interview-based medical exams using questionnaires and fever checks with thermography. However, because the former method relies on voluntary cooperation from people entering the country, false statements are a possibility, and the latter method has its own limits, for example, it does not cover passengers who have taken antifebrile medication. To overcome these challenges in quarantine inspections, Matsui and Sun et al. are developing infectious-disease screening systems using multiple biosensors that measure vital signs to identify symptomatic people [5, 6]. As a result of being infected, not only body temperature but also heart and respiration rates increase. The system automatically detects infected individuals within 15 s by a discriminant function using measured vital signs. Heart and respiration rates are determined using a microwave radar by noncontact way, and facial skin temperature is monitored by a thermographic camera. By using these three parameters, the detection accuracy of the system improved ranged from 81.5 to 98.0% in case-control studies. This is notably higher compared to the conventional screening methods using only thermography.

Considering future practical applications for infectious-disease screening systems, it would be beneficial to build infectious-disease screening systems powered by image analysis using infrared cameras [12]. There are four reasons for this. (1) Infrared cameras are already used at airport quarantine stations around the world and are extremely versatile. (2) It is possible to measure vital signs by simply changing a camera's software. (3) When vital signs can be measured, and symptomatic people identified by taking images with just a camera, the need

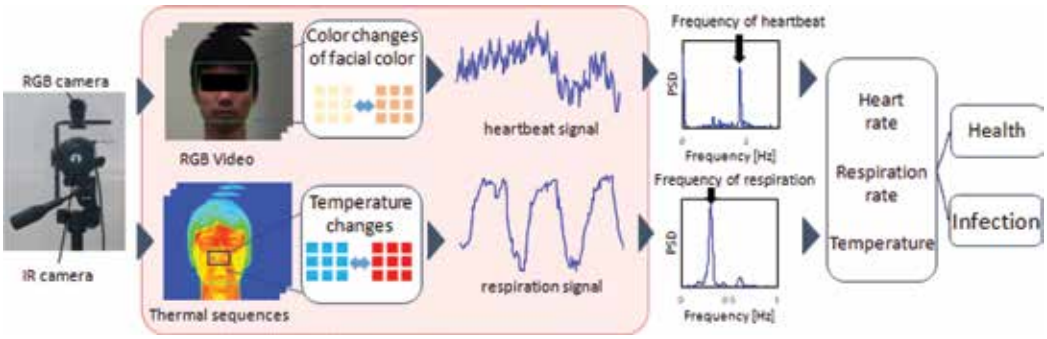

Figure 5. The infectious disease screening system using infrared/RGB facial-image analysis.

for quarantine can be determined using existing equipment without the need to bring in new devices. (4) There is a lower risk of secondary infection caused by contact with equipment, such as measurement devices.

A clinical evaluation was conducted to confirm the accuracy of identifications made by an infectious-disease screening system using infrared/RGB facial-image analysis (**Figure 5**). We used an infrared RGB camera to measure facial surface temperature, respiratory rate, and heart rate over a period of 10 s in a symptomatic group of 16 people (average age 36.6 ± 14.1) diagnosed with influenza A (seven people) or influenza B (nine people) by a physician. The same measurements were taken in a healthy group of 22 people (average age 43 ± 18.7). The identification accuracy was verified by conducting a logistic regression analysis of the symptomatic and healthy groups based on the subjects' body surface temperature, respiratory rate, and heart rate measured using image analysis:

$$Z(x_1, x_2, x_3) = \log\left(\frac{p_i}{1-p_i}\right) = -203.27 + 0.49\,x_1 + 0.36\,x_2 + 4.68\,x_3 \quad (2)$$

Here, $Z_{(x_1, x_2, x_3)} = \log\left(\frac{p_i}{1-p_i}\right)$ is the identification score, x_1 is respiratory rate, x_2 is heart rate, and x_3 is the body surface temperature. The results of the identification were as follows: false negatives in two subjects produced misclassification, sensitivity was 87.5%, specificity was 100%, positive predictive value (PPV) was 100%, and negative predictive value (NPV) was 91.7%.

The goal of this study was to develop an infectious-disease screening system using infrared/RGB facial-image analysis. Furthermore, to make this system a reality, we verified the accuracy and clinically evaluated measurement of respiratory rate and heart rate using infrared/RGB images. The results confirmed that measuring respiratory rate and heart rate using infrared/RGB analysis makes highly accurate measurement possible.

5. Conclusion

This chapter introduced the principles behind noncontact measurement of respiration and heartbeat using infrared/RGB facial-image analysis, and the applications for such measurement

in the detection of patients suspected to have an infectious disease were explored. Looking toward future practical applications, elimination of noise caused by body movement and a face/nose tracking function for automatic measurement of heart and respiratory rates will likely be added, improving the accuracy and stability of measurements, and we can expect this technology to be applied in a variety of ways.

Acknowledgements

This research was supported by a Grant-in-Aid for Young Scientists (16K16363) founded by the Ministry of Education, Culture, Sports, Science and Technology of Japan.

Conflict of interest

The authors declare no conflicts of interest.

Author details

Guanghao Sun[1]*, Toshiaki Negishi[1], Tetsuo Kirimoto[1], Takemi Matsui[2] and Shigeto Abe[3]

*Address all correspondence to: guanghao.sun@uec.ac.jp

1 Graduate School of Informatics and Engineering, The University of Electro-Communications, Tokyo, Japan

2 Graduate School of System Design, Tokyo Metropolitan University, Tokyo, Japan

3 Takasaka Clinic, Fukushima, Japan

References

[1] Yao Y, Brüser C, Pietrzyk U, Leonhardt S, Waasen S, Schiek M. Model-based verification of a non-linear separation scheme for ballistocardiography. IEEE Journal of Biomedical and Health Informatics. 2014;**18**(1):174-182. DOI: 10.1109/JBHI.2013.2261820

[2] Li C, Lin J. Microwave Noncontact Motion Sensing and Analysis. 1st ed. NJ, USA: John Wiley & Sons; 2013

[3] Matsui T, Yoshida Y, Kagawa M, Kubota M, Kurita A. Development of a practicable non-contact bedside autonomic activation monitoring system using microwave radars and its clinical application in elderly people. Journal of Clinical Monitoring and Computing. 2013;**27**(3):351-356. DOI: 10.1007/s10877-013-9448-3

[4] Kagawa M, Tojima H, Matsui T. Non-contact diagnostic system for sleep apnea-hypopnea syndrome based on amplitude and phase analysis of thoracic and abdominal Doppler radars. Medical and Biological Engineering and Computing. 2015;**54**(5):789-798. DOI: 10.1007/s11517-015-1370-z

[5] Sun G, Matsui T, Hakozaki Y, Abe S. An infectious disease/fever screening radar system which stratifies higher-risk patients within ten seconds using a neural network and the fuzzy grouping method. Journal of Infection. 2015;**70**(3):230-236. DOI: 10.1016/j.jinf.2014.12.007

[6] Matsui T, Hakozaki Y, Suzuki S, Usui T, Kato T, Hasegawa K, et al. A novel screening method for influenza patients using a newly developed non-contact screening system. Journal of Infection. 2010;**60**(4):271-277. DOI: 10.1016/j.jinf.2010.01.005

[7] Sun G, Shinba T, Kirimoto T, Matsui T. An objective screening method for major depressive disorder using logistic regression analysis of heart rate variability data obtained in a mental task paradigm. Frontiers in Psychiatry. 2016;**7**:180. DOI: 10.3389/fpsyt.2016.00180

[8] Poh M, McDuff D, Picard R. Advancements in noncontact, multiparameter physiological measurements using a webcam. IEEE Transactions on Biomedical Engineering. 2011;**58**(1):7-11. DOI: 1109/TBME.2010.2086456

[9] Allen J. Photoplethysmography and its application in clinical physiological measurement. Physiological Measurement. 2007;**28**(3):R1-R39

[10] Allen J, Murray A. Effects of filtering on multisite photoplethysmography pulse waveform characteristics. Computers in Cardiology. 2004;**31**:485-488. DOI: 10.1109/CIC.2004.1442980

[11] Nakayama Y, Sun G, Abe S, Matsui T. Non-contact measurement of respiratory and heart rates using a CMOS camera-equipped infrared camera for prompt infection screening at airport quarantine stations. In: Proceedings of the IEEE International Conference on Computational Intelligence and Virtual Environments for Measurement Systems and Applications (CIVEMSA); 12-14 June 2015; Shenzhen. DOI: 10.1109/CIVEMSA.2015.7158595

[12] Sun G, Nakayama Y, Dagdanpurev S, Abe S, Nishimura H, Kirimoto T, et al. Remote sensing of multiple vital signs using a CMOS camera-equipped infrared thermography system and its clinical application in rapidly screening patients with suspected infectious diseases. International Journal of Infectious Diseases. 2017;**55**:113-117. DOI: 10.1016/j.ijid.2017.01.007

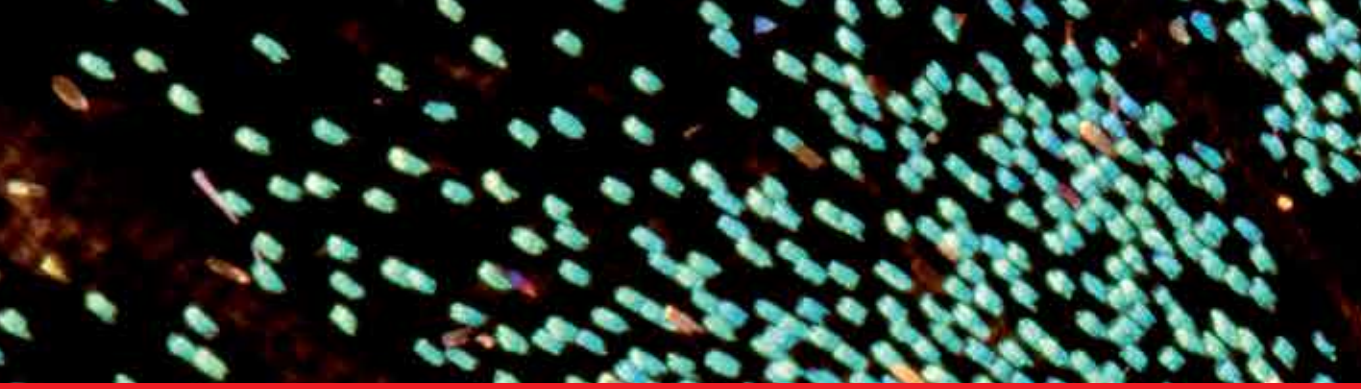

Edited by Mariusz Marzec and Robert Koprowski

The main themes of the book are the broadly understood methods of image analysis and processing applied to support diagnosis and therapy, but also to assess the implants placed in the patient's body and the related treatment processes. The examples concern processing and analysis of images or measured signals obtained from various diagnostic imaging methods. The study used, among others, standard X-ray images, computed tomography images, microtomographic images, as well as thermographic and ultrasound images. The results of image and signal processing were used in medical diagnosis and to evaluate the effectiveness of therapy. The material contained in this book may be of interest to a wide audience, and the discussed topics cover the current state of knowledge on the use of image processing algorithms in medicine and related fields.

ISSN 2631-5343
ISBN 978-1-83881-837-1

Published in London, UK

IntechOpen